CONSTITUTIVE PARAMETER MEASUREMENT USING DOUBLE RIDGE

WAVEGUIDE

THESIS

Nathan J. Lehman, Captain, USAF

AFIT-ENG-13-M-30

DEPARTMENT OF THE AIR FORCE
AIR UNIVERSITY

AIR FORCE INSTITUTE OF TECHNOLOGY

Wright-Patterson Air Force Base, Ohio

CONSTITUTIVE PARAMETER MEASUREMENT USING DOUBLE RIDGE

WAVEGUIDE

THESIS

Presented to the Faculty

Department of Electrical and Computer Engineering

Graduate School of Engineering and Management

Air Force Institute of Technology

Air University

Air Education and Training Command

in Partial Fulfillment of the Requirements for the

Degree of Master of Science in Electrical Engineering

Nathan J. Lehman, B.S.E.E.

Captain, USAF

March 2013

CONSTITUTIVE PARAMETER MEASUREMENT USING DOUBLE RIDGE

WAVEGUIDE

Nathan J. Lehman, B.S.E.E.
Captain, USAF

Approved:

_____   _____

Michael Havrilla, PhD (Chairman)   Date

_____   _____

Maj Milo Hyde, PhD (Member)   Date

_____   _____

Peter Collins, PhD (Member)   Date

AFIT-ENG-13-M-30

Abstract

Electromagnetic materials characterization is important in the design of systems that interact with electromagnetic waves. Determining the constitutive parameters of a material is a vast area of research and practice. For this paper, discussion will focus on a destructive method using waveguides in the frequency range of 6-18 GHz. Traditional methods to perform similar measurements include using coaxial cable, stripline, focus beam and rectangular waveguides. This work will use Double Ridged Waveguide (DRWG) to compare to these other methods and will discuss the attributes and drawbacks of this new approach. The most similar method utilizes rectangular waveguide, so the primary focus will be on comparisons this method with DRWG. The significant advantage to using DRWG is the increase in available measurement bandwidth. The challenges include sample fabrication and increased mathematical difficulty in finding the cutoff frequency for DRWG. These challenges are addressed and measurement results are examined.

To my wife, my daughters and my father. Thank you for the love and support.

Acknowledgments

I would like express my gratitude to Dr. Michael Havrilla, my research advisor. Your ability to illustrate the entire picture of the subject was critical to the success I had in my experience here.

Thank you to Maj Milo Hyde and Dr. Peter Collins for your work in helping to make my entire graduate school experience a unique learning opportunity. The contrasting methods of presenting material was helpful to understanding material.

Thank you to Dr. Robert Schill Jr. for the opportunity you provided me to assist in your laboratory. I still enjoy reflecting on that time and experience as further motivation to study electromagnetics.

Thank you to Dr. William Baker for your assistance in offering another perspective on the mathematics presented here. While the destination was the same, the alternate path was vital to understanding.

Also, thank you to Mr. Charles McNeely for your patience and assistance, despite my repeated attempts to break equipment in your laboratory.

Finally, I would like to thank my classmates for your continued support and friendship during our time at AFIT. I consider myself extremely fortunate to have been affiliated with you gentlemen through this challenge. Nice work guys!

Nathan J. Lehman

Table of Contents

List of Figures

List of Tables

List of Acronyms

Acronym	Definition
AFRL	Air Force Research Laboratory
AFIT	Air Force Institute of Technology
DRWG	Double Ridged Waveguide
LO	Low Observable
NRW	Nicholson-Ross-Weir
NWA	Network Analyzer
PEC	Perfect Electric Conductor
RAM	Radar Absorbing Material
TEM	Transverse Electromagnetic
TE	Transverse Electric
TM	Transverse Magnetic
TRL	Thru-Reflect-Line

CONSTITUTIVE PARAMETER MEASUREMENT USING DOUBLE RIDGE
WAVEGUIDE

I. Introduction

MEASUREMENT of a material's constitutive parameters are important to the design and maintenance of any system that will interact with electromagnetic waves. Determining these parameters can be especially useful in Low Observable (LO) aircraft platforms for diagnosis and health status of the Radar Absorbing Material (RAM) treatments. The constitutive parameters can vary with frequency, thus providing a challenge for measurements. The measurement techniques used need to be selected in accordance with the material and scenario in which the measurement is taking place. The technique explored in this thesis will utilize a Network Analyzer (NWA) and waveguides. Traditionally, rectangular waveguide is used since its electromagnetic properties are well known and the mathematical model is well understood; however, the measurement bandwidth is narrow. To gain a larger bandwidth, this thesis will explore the use of Double Ridged Waveguide (DRWG) in place of rectangular waveguide. The scope and limitations of using DRWG will be compared with other methods of measurement.

1.1   Problem Statement

While the NWA is capable of recording measurements across a large frequency range, the transmission line can limit the available bandwidth. For the well known measurement method of using rectangular waveguides, the waveguide itself is the limiting component. In order to acquire a broad band of measurements with rectangular waveguide, multiple sizes of waveguide and corresponding material samples must be used. Using a different

geometry of waveguide, such as Double Ridge Waveguide (DRWG), can provide a larger bandwidth of wave propagation from the same guide [3, 11]. The increased bandwidth can provide higher resolution for detection of defects in RAM, thus providing a more cost effective tool used in coating diagnosis. An example of both geometries is shown in Figure 1.1. While replacing the rectangular waveguide with DRWG will expand bandwidth, new challenges such as sample fabrication and NWA calibration are introduced. Additionally, the mathematical modeling of a DRWG is more difficult. To ensure accuracy, an in depth analysis of a NWA calibration scheme will need to be investigated as well as exploring material fabrication challenges.
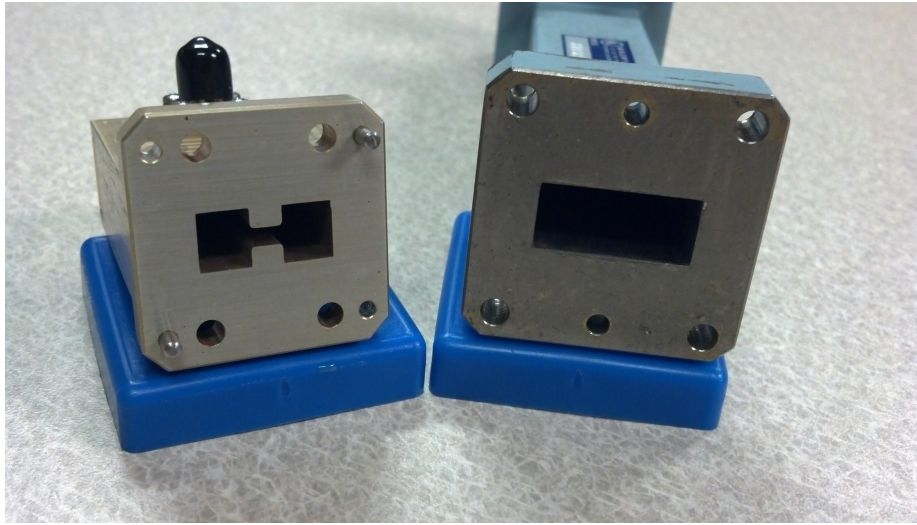
Figure 1.1: Double Ridge Waveguide (left) and Rectangular Waveguide (right)

1.2   Limitations and Challenges

A limitation of using DRWG for materials measurements is the same as any other waveguide system; the bandwidth will still be limited [15]. Even though a single DRWG can significantly increase the measurement bandwidth compared to rectangular waveguides, measurements could be desired in a much larger band. Additionally, low frequency measurements are extremely difficult to attain using waveguide methods, as the

waveguide dimensions become very large. Two challenges arise as a direct result of the complex shape: sample fabrication and mathematical modeling of wave propagation in the guide. Samples are placed in a holder that has the same shape and dimensions as the waveguide itself. The sample should fill the waveguide completely, so the geometry for DRWG is clearly more complex than that of rectangular waveguide and some materials may not be easily formed to the correct shape. The mathematical description of the electromagnetic boundary conditions give rise to a much more intense analysis, necessary to determine the constitutive parameters.

A practical limitation of taking measurements with this method is that it is fundamentally destructive in nature. While the sample being measured may not be damaged, the shape must be harvested from the original test article. For example: If a measurement of an aircraft's RAM coating is desired, the sample will need to be cut from the aircraft, thus damaging the LO treatment. This work will provide a proof of concept in order to further research non-destructive techniques that are extremely useful in LO aircraft diagnosis.

1.3 Scope

Waveguides, both rectangular and double ridged, can be purchased in a variety of different sizes and dimensions. In inventory at AFIT are rectangular waveguide measurement devices that operate in the X-Band range (8-12GHz). To accomplish relevant comparisons between the two different waveguides, a frequency band of about 6-18GHz has been chosen to prove the concept. This frequency range is commercially available as a WRD-650 double ridged waveguide. This range will span a portion of the C-band (5.85-8.2GHz) and include all of the X, and Ku (12.4-18GHz) bands of frequencies. Measurements will be compared among rectangular and DRWG for validation, even though rectangular waveguide requires three bands to span the entire DRWG bandwidth.

1.4 Research Goals

As stated, the primary goal of this research is to acquire the ability to make broadband material measurements from a single material sample. The broader goal is to save time in performing these measurements and reduce the amount of samples necessary. New measurement tools, such as MATLAB code to externally calibrate data, would be important to future work in this field. Investigation on material shape effects in DRWG is desired, since the existing requirement is difficult to fabricate compared to traditional rectangular waveguide samples. The uncertainty and effects of imperfect material samples will be investigated as well. While the mathematical model of DRWG has been addressed [15, 20], it is the goal of this thesis to perform a more descriptive method. The primary output of the mathematical methods that this thesis is interested in is the cutoff wavenumber (k_c) or frequency (f_c), which are related.

1.5 Resource Requirements

Comparing the results of using DRWG to rectangular waveguide will verify that the methods used are valid. To make this comparison, it will be necessary to have all the equipment required to accomplish both types of measurements. The resources necessary to complete the objective related to this thesis are as follows:

- MATLAB software for external calibration,

- Network Analyzer to take measurements,

- Rectangular waveguide with associated coaxial cable adapter (2),

- Double ridged waveguide with associated coaxial cable adapter (2),

- Double ridged line standard to verify methodology,

- Coaxial cabling with SMA connectors to connect the measurement guides (2),

- Metal short plate for ends of waveguides for reflect calibration,

- Material samples in rectangular shape for comparison,

- Material samples in double ridged shape for verification of methodology.

1.6 Organization

This thesis is divided into five chapters. The second chapter will go over basic electromagnetic and material concepts, scattering parameters, waveguide propagation fundamentals and will include an overview of the NWA with associated calibration schemes. The third chapter will derive the cutoff frequency for DRWG, explore the Nicholson-Ross-Weir (NRW) method for determining the constitutive parameters, and discuss sample preparation. The fourth chapter will discuss results relating to the constitutive parameters, uncertainty, sample modifications and comparisons to rectangular waveguide measurements. The fifth chapter will summarize the work performed for this thesis and discuss any changes or improvements for future work.

II.   Background

To better appreciate the ability to take measurements of the constitutive parameters of a material, a conceptual knowledge of the principles involved is important. Becoming familiar with existing measurement methods is important to understanding the methods presented in this thesis. This chapter will discuss electromagnetic properties, material concepts, waveguide fundamentals, alternate measurement techniques and the calibration method.

2.1   Basic Electromagnetic Principles and Maxwell's Equations

Electromagnetics is the study of systems of charge in a general state of motion [3]. While many scientists have contributed to the modern field of electromagnetic theory, the basis equations for study are known as Maxwell's equations. They describe the behavior of electromagnetic waves and are represented in either integral of differential form. While examination of Maxwell's equations is broad in scope, this thesis will focus on specific attributes and can be summarized succinctly. In the following sections, important concepts such as duality, electric and magnetic fields, mono-poles and dipoles will be reviewed. Some common symbols used in this thesis are:

- **E** - Electric Field Intensity (volts/meter)

- **H** - Magnetic Field Intensity (amperes/meter)

- **D** - Electric Flux Density (coulombs/square meter)

- **B** - Magnetic Flux Density (webers/square meter)

- **J** - Electric Current Density (amperes/square meter)

- $\mathfrak{M}$ - Magnetic Current Density (volts/square meter)

These symbols are denoted as vector quantities and are assumed to be time varying.

2.1.1 Duality.

In mathematics, if two equations have the same form, their solutions will also have the same form. This concept is called duality. To demonstrate this principle, a comparison of the Maxwell-Faraday equation and Ampere's Law can be used:

$$\nabla \times \mathbf{E} = -\mathfrak{M} - \frac{\partial \mathbf{B}}{\partial t} \tag{2.1}$$

$$\nabla \times \mathbf{H} = \mathbf{J} + \frac{\partial \mathbf{D}}{\partial t}. \tag{2.2}$$

Observing that (2.1) and (2.2) have similar forms, duality can be applied. This principle is important in the study of electromagnetics as one can have the solution to one type of problem, and interchange the symbols to have the solution to another problem [11].

The premise of using duality in Maxwell's equations assumes an existence of magnetic current density ($\mathfrak{M}$) and thus magnetic charges. Physically these entities have not been shown to exist, but can be of great assistance in the analysis and study of electromagnetics [3]. Physically, an electric charge does exist. Gauss's Law for $\mathbf{D}$ and $\mathbf{B}$ is written as,

$$\nabla \cdot \mathbf{D} = q_{ev} \tag{2.3}$$

$$\nabla \cdot \mathbf{B} = q_{mv} \tag{2.4}$$

where q_{ev} is electric charge and q_{mv} is the magnetic charge. In most cases, the magnetic charge can be set to zero although sometimes it is beneficial to leave it as a variable so duality or equivalence principles can more easily be observed and applied [18].

2.2 Types of Materials

Atomic composition determines the type of interaction a material will exhibit in the presence of an electric or magnetic field. The characteristics of this interaction describe the properties of the material. These properties are important to consider when analyzing a phenomenon or attempting to design a product. The primary categories explored in this thesis are conductors, dielectrics and magnetics, but others exist [3].

2.2.1 Conductors.

The outer shell of an atom is known as the valence shell. Electrons that occupy this shell are known as valence electrons. For electromagnetic interaction purposes, this shell is of prime interest. If there are unmatched valence electrons, they are known as "free" electrons. If a material is comprised of molecules with a lot of free electrons, it is called a conductor. In conductors, the electrons can move in random directions and different velocities with no field applied. Movement of electrons is known as current and with no field applied, the net current will be zero in the conductor [3]. When a field is applied, these free electrons will move with a direction and velocity relative and proportional to the field vector. The measure of how susceptible a material is to supporting an electric or magnetic current is called *Conductivity* and is denoted by σ.

2.2.2 Dielectrics.

As opposed to conductors, an ideal dielectric does not have free electrons available to move. Instead of conducting a current in the presence of an applied field, these materials distort or change shape. This resultant distortion is known as a dipole. While dipoles do have a field associated with them, they are randomly oriented and distributed throughout a material and will create a net field of zero. When a field is applied to an ideal dielectric the dipoles may align themselves with the field vector, known as polarization, but will not allow transfer of electrons. The measure of how susceptible a material is to becoming polarized is called *Permittivity* and is denoted by ϵ [11].

2.2.3 Magnetics.

Magnetics are essentially the dual of dielectrics mathematically. Physically, they are different for the same reasons described in Section 2.1.1. Instead of a simple polarization and corresponding electric field, magnetic materials experience a torque. Thinking of dipoles as electric current loops instead of dipoles can help to understand this concept as shown in Figure 2.1. The torque follows the right hand rule similar to the concept of

moment of inertia in the physics of motion. When the moment vectors all point in the same direction, the material is said to be magnetized. The measure of how susceptible a material is to becoming magnetized is called *Permeability* and is denoted by μ [3].
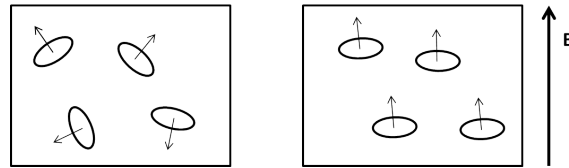
Figure 2.1: Magnetic Loop Illustration: No Magnetic Field (left) and Magnetic Field Applied (right)

2.3   The Constitutive Parameters

The conductivity, permittivity and permeability of a material are collectively known as the constitutive parameters. These parameters characterize the interaction of electric and magnetic fields with the material. When applying Maxwell's Equations, (2.1) through (2.4), the constitutive parameters can be used to make some relations. The equations that demonstrate the relations are called the "Constitutive Relations" [11] and are written as,

$$\mathbf{J} = \sigma\mathbf{E} \tag{2.5}$$

$$\mathbf{D} = \epsilon\mathbf{E} \tag{2.6}$$

$$\mathbf{B} = \mu\mathbf{H}. \tag{2.7}$$

Since the materials studied here will be classified largely as dialectics, only the permittivity and permeability will be emphasized. Further use of the term "constitutive parameters" will imply only these two parameters. Because they are meant to describe the medium in which the field exists, permittivity and permeability can be decomposed to

9

differentiate between free space and a material:

$$\epsilon = \epsilon_r \epsilon_0 \qquad (2.8)$$

$$\mu = \mu_r \mu_0, \qquad (2.9)$$

where ϵ_r and μ_r are permittivity and permeability relative to the material and ϵ_0 and μ_0 are indicative of free space. The free space parameters have the approximate and defined values

$$\epsilon_0 \cong 8.854 \times 10^{-12} \ \ \text{(farads/meter)} \qquad (2.10)$$

$$\mu_0 \triangleq 4\pi \times 10^{-7} \ \ \text{(henry/meter)}. \qquad (2.11)$$

The permeability of free space is defined to be the above value. It can be related to the free space permittivity by

$$\epsilon_0 = \frac{1}{c^2 \mu_0}, \qquad (2.12)$$

where c is the measured speed of light ($\sim 2.99792 \ ^\text{m}/_\text{s}$).

For the analysis performed in this work, the constitutive parameters are not directly measured. Instead, the scattering (or S) parameter data is taken from the NWA. Later on, the NRW algorithm is used to derive the constitutive parameters from the S-parameters.

2.4   Scattering Parameters

The overall goal of this research effort is to find the constitutive parameters of a material. Because the network analyzer does not measure these parameters directly, it is vital to understand what measurements are actually taken. The S-parameters are measured over a spectral range by the network analyzer. By conservation of energy, a wave can either transmit through, be absorbed into, or reflect from a material [11]. A graphical representation of reflection and transmission is shown in Figure 2.2.   A simple method of describing this interface is by utilizing the scattering matrix. It is possible to relate the waves transmitted and reflected on the right side in Figure 2.2, to the waves on the left

10
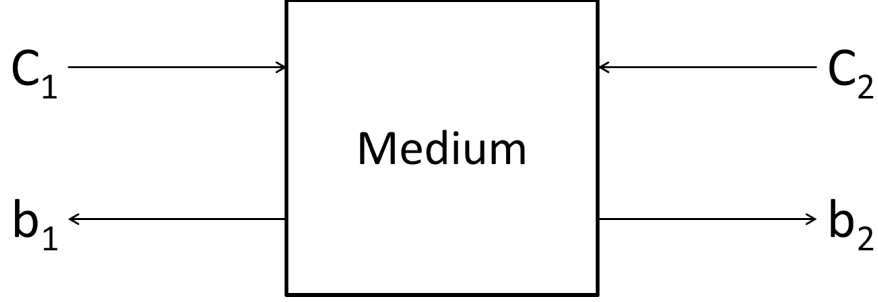
Figure 2.2: Material Interface Model

side with. The relation is accomplished with the scattering parameters [8]. A mathematical representation of a material interface is shown by

$$b_1 = c_1 S_{11} + b_2 S_{12} \tag{2.13}$$

$$c_2 = c_1 S_{21} + b_2 S_{22}. \tag{2.14}$$

Rewriting in a matrix form,

$$\begin{bmatrix} b_1 \\ c_2 \end{bmatrix} = \begin{bmatrix} S_{11} & S_{12} \\ S_{21} & S_{22} \end{bmatrix} \begin{bmatrix} c_1 \\ b_2 \end{bmatrix} \tag{2.15}$$

where S_{11} and S_{22} are the reflection coefficients from the right and left sides respectively. S_{21} and S_{12} are the transmission coefficients from the right and left sides respectively. These coefficients are collectively referred to as the S-parameters, and are represented as complex numbers to indicate magnitude and phase.

Observation of (2.15) shows that the left side of the matrix equation does not correspond to the left side of Figure 2.2. To simplify analysis, the T-parameters can be introduced. T-parameters can mathematically depict the Figure 2.2 by,

$$\begin{bmatrix} b_1 \\ c_1 \end{bmatrix} = \begin{bmatrix} T_{11} & T_{12} \\ T_{21} & T_{22} \end{bmatrix} \begin{bmatrix} b_2 \\ c_2 \end{bmatrix}. \tag{2.16}$$

The conversion from S to T parameters is discussed in Section 2.8. One of the advantages to using the T-parameters is the simplicity in representing a network consisting of multiple

11

layers. The T-matrices can be written as matrix multiplication with a T-matrix representing each layer. For example, if Figure 2.2 included n number of blocks representing different mediums, then the system could be represented mathematically as:

$$\begin{bmatrix} T_{11}^T & T_{12}^T \\ T_{21}^T & T_{22}^T \end{bmatrix} = \begin{bmatrix} T_{11}^1 & T_{12}^1 \\ T_{21}^1 & T_{22}^1 \end{bmatrix} \begin{bmatrix} T_{11}^2 & T_{12}^2 \\ T_{21}^2 & T_{22}^2 \end{bmatrix} \dots \begin{bmatrix} T_{11}^n & T_{12}^n \\ T_{21}^n & T_{22}^n \end{bmatrix} \tag{2.17}$$

2.5 Waves and Waveguide Propagation

To better understand the discussion, a brief overview of the type of waves is provided here. The first concept is wave modes and polarization. The modes discussed will include Transverse Electromagnetic (TEM), Transverse Electric (TE) and Transverse Magnetic (TM). A TEM wave is described a wave where both **E** and **H** are contained in a plane transverse to the direction of propagation. This type of wave can exist in free space or in a guide with two separate conductors. A TE wave refers to the **E** field in the plane transverse to the direction of propagation. Finally, a TM wave contains the **H** field in the plane transverse to the direction of propagation [3].

In order to solve for the constitutive parameters, the cutoff wavenumber (or frequency) is needed for the NRW discussed later. A cutoff frequency is the frequency below which a wave ceases to propagate in a waveguide for a given propagation mode [11]. This thesis is exploring DRWG as a measurement apparatus, but the technique is similar to using rectangular waveguides. The mathematical goal of finding the cutoff wavenumber is fairly straightforward with regard to rectangular waveguide. For this analysis it can be assumed that the wave will be a TE^z wave, meaning it is a TE wave with propagation in the z-direction. The **E** and **H** fields are desired, but are extremely difficult to solve for directly. It is common practice to use the vector potentials **A** (magnetic vector potential) and **F** (electric vector potential) to aid in the analysis [4]. For this analysis,

$$\mathbf{F} = \hat{z} F_z \tag{2.18}$$

$$\mathbf{A} = 0 \tag{2.19}$$

12

where F_z is the z component of the potential. For any propagating wave in a source free region, the Helmholtz Wave Equation must be satisfied

$$\nabla^2 F_z + k^2 F_z = 0 \qquad (2.20)$$

where k is the wavenumber. For a wave standing in the x and y directions and traveling in the z direction,

$$F_z = (A \cos k_x x + B \sin k_x x)(C \cos k_y y + D \sin k_y y)(E e^{-jk_z z} + F e^{jk_z z}) \qquad (2.21)$$

where A,B,C,D,E, and F are constants to be solved for and $j = \sqrt{-1}$. Now that the vector potentials are known, the $\mathbf{E}$ and $\mathbf{H}$ fields can be solved for. The equations relating the fields to the vector potentials are

$$\mathbf{E} = \frac{1}{j\omega\epsilon\mu}\left[k^2 \mathbf{A} + \nabla(\nabla \cdot \mathbf{A})\right] - \frac{\nabla \times \mathbf{F}}{\epsilon} \qquad (2.22)$$

and

$$\mathbf{H} = \frac{\nabla \times \mathbf{A}}{\mu} + \frac{1}{j\omega\epsilon\mu}\left[k^2 \mathbf{F} + \nabla(\nabla \cdot \mathbf{F})\right]. \qquad (2.23)$$

Unique solutions will be dependent on boundary conditions and wave mode. The boundary conditions can be solved for in terms of the mode numbers. While an infinite number of modes can exist, the lowest order (or dominant) mode for rectangular waveguide is known as the "1-0" mode, notated as TE_{10}^z. Detectors in the NWA used in this work detect this dominate mode, so it is of particular interest [3].

2.5.1 Rectangular Waveguide.

Using the assumption that a waveguide is constructed using a Perfect Electric Conductor (PEC) material and it has dimensions a and b, the cutoff frequency can be shown to be given by

$$f_{mn}^c = \frac{1}{2\pi \sqrt{\epsilon\mu}} \sqrt{\frac{m^2\pi^2}{a^2} + \frac{n^2\pi^2}{b^2}} \qquad (2.24)$$

where n and m describe the mode [11]. A convenient property of rectangular waveguide is the ability to express the cutoff frequency in closed form. As derived in later analysis, this

13

is not possible for DRWG. In addition to cutoff frequency information, it is important to understand how the fields are distributed in the cross section of the guide.

2.5.2   Field Behavior.

For rectangular waveguide, the electric field inside the guide can be described as sinusoidally distributed along the x-axis, oriented in the y-direction [3]. With respect to material measurements performed in rectangular waveguide, the sample should fill the entire guide completely.

For DRWG, the fields are highly concentrated at the corners of the ridge [20]. While measurement error will occur if the material does not completely fill the guide, it stands to reason that large errors would be expected if any gaps exist in the vicinity of the corners of the ridge. This error will be explored in a later chapter.

2.6   Measurement Bandwidth

As stated, the primary advantage to using DRWG over rectangular waveguide is the increased bandwidth. Table 2.6 shows an example of manufacturer supplied bandwidth capabilities for some example waveguides [14] [6]. As can be seen, it will take approximately three rectangular waveguides to accomplish the same measurement as one DRWG. Some verification of this information will be explored in later chapters.

Table 2.1: Waveguide Bandwidth

Waveguide Type	Model	Bandwidth
Rectangular (C-Band)	WR-137	5.85-8.20
Rectangular (X-Band)	WR-90	8.20-12.40
Rectangular (Ku-Band)	WR-62	12.40-18.00
DRWG	WRD-650	6.5-18.00

2.7   Other Measurement Methods

This thesis focuses on waveguide measurements that support TE or TM propagation modes only. There are more techniques that can be utilized to derive the constitutive parameters while performing similar measurement methods, with respect to similar algorithms. Three other methods include stripline, focus beam and coaxial techniques. The devices used in these alternate methods can support a TEM wave in addition to TE or TM modes.

2.7.1   Coaxial Cable.

Coaxial cables are used commonly in a vast array of applications due to their ease of use, variety of connectors, relatively robust design and most importantly, large bandwidth. This type of transmission line consists of a center conductor surrounded by a dielectric material and then encased in another conductor [5]. An example is shown in Figure 2.3. Because of the ability to transmit TEM waves, the bandwidth of coaxial cabling can be extremely large. The lower limit is theoretically DC while the upper limit is determined by the excitement of higher order modes. One major drawback to using coaxial cable for constitutive parameter measurements is the discontinuity of the radial electric field [2]. If an air gap exists between the center conductor and the sample under test, the uncertainty in
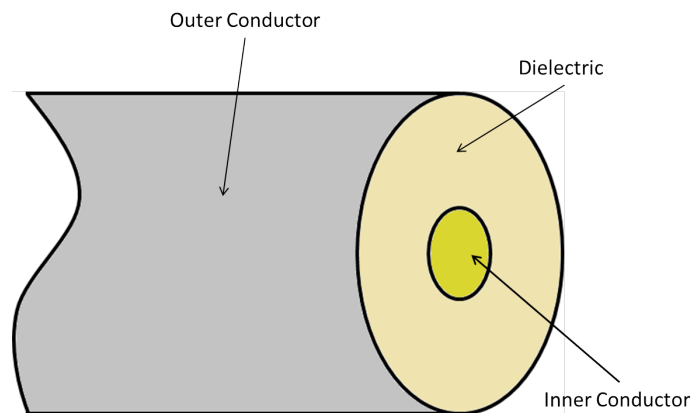
Figure 2.3: Diagram of Coaxial Cable

15

the measurement grows large. Coaxial cable measurements can also suffer from inaccuracy due to poor field penetration into the material [5].

2.7.2 Stripline.

Stripline is a type of planar transmission line, analogous to coaxial cable without the outer conductor completely surrounding the dielectric material, as seen in Figure 2.4. It is constructed of two plates with a conductor running lengthwise in the center. Also similar to coaxial cable, stripline supports TEM wave propagation modes and is band-limited for the same reasons. The method used to make material measurements in a stripline is to form a material sample around the center conductor. Again there is a significant challenge to designing a material sample to fit this area. Gaps between the conductors (inner or outer) and the material will cause uncertainty in measurement similar to coaxial cable.
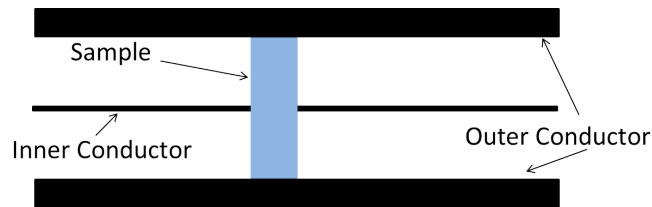
(a) Diagram
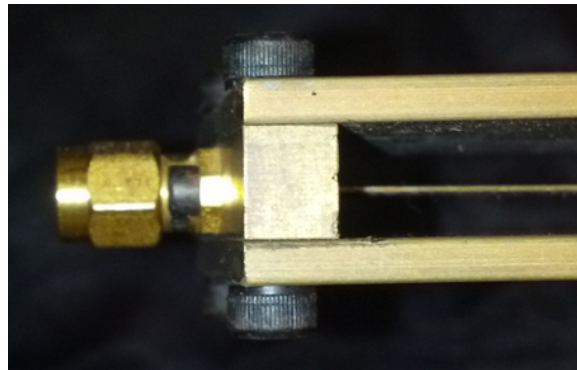
(b) Picture

Figure 2.4: Stripline Diagram and Picture

2.7.3   Focus Beam.

The focus beam system consists of horn antennas, lenses and a sample holder to make measurements (Figure 2.5). The horn antennas launch a spherical wave to the lenses, that in turn, transform the wave into a plane wave [10]. Because of the equiphase and equiamplitude characteristics, plane waves make deriving the intrinsic wave properties easier, thus producing a measurement from the material interaction [3, 10, 16]. Sample fabrication is more easily accomplished for the focus beam system with the trade off being complications of taking a measurement. Some additional advantages of the focus beam system is the ability to take off normal or oblique measurements, and the ability to heat the sample since it doesn't touch any waveguide [5]. Calibration of the system requires the lenses, the sample and sample holder to exist at exact known locations. Additionally, scattering from the sample holder and other "clutter" sources can be introduced into the measurement because the system is not contained like coaxial cable, stripline or waveguide [10]. Accurate measurements require extremely good control of the environment surrounding the system and accurate calibration techniques. Sample sizes can also be a limiting factor. The bandwidth is determined by the physical dimensions of th lenses (lower limit) and the antennas or cabling (upper limit).
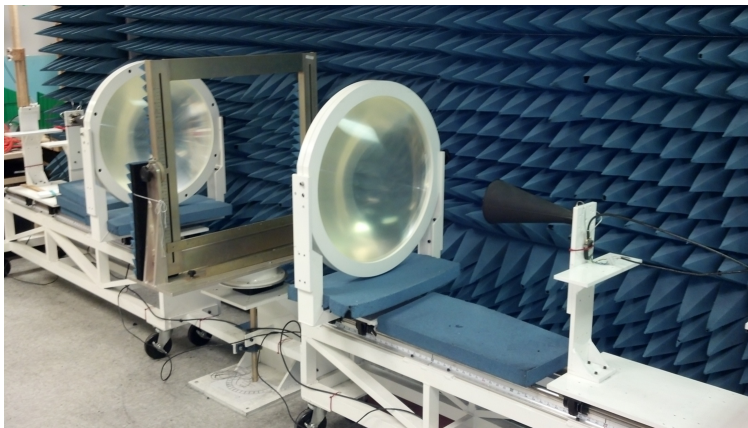
Figure 2.5: Picture of Focus Beam Measurement System

2.8 Network Analyzer Operation and Calibration

A rough diagram of a materials measurement configuration is shown in Figure 2.6(a). The detectors that perform the actual measurements are contained inside the NWA. Everything that electrically connects the detectors to each other must be mathematically accounted for. A block diagram characterizing this system is shown in Figure 2.6(b).
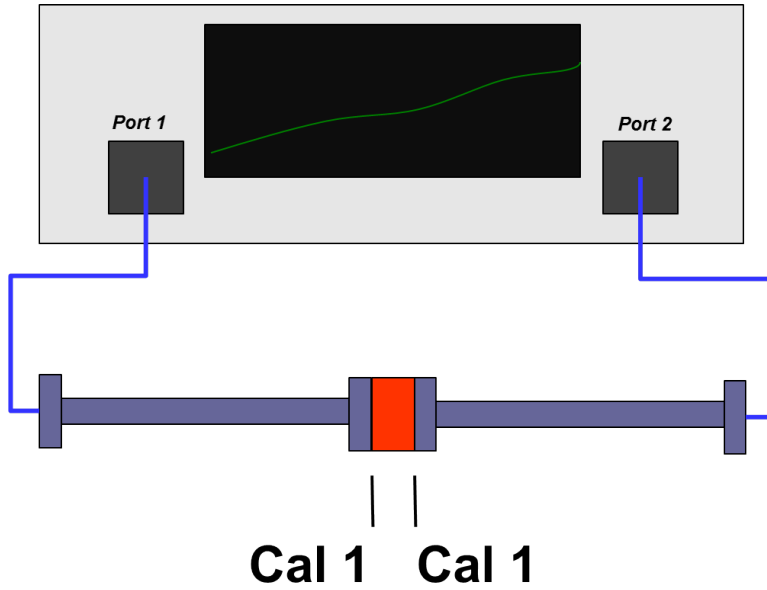
(a) Network Analyzer
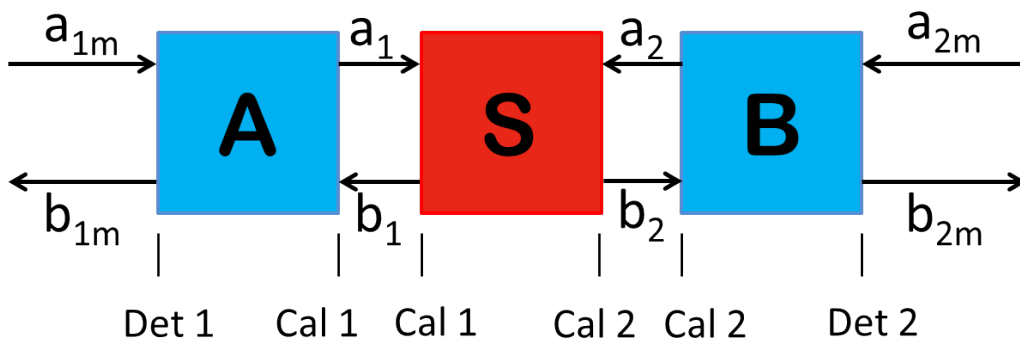
(b) NWA Block Diagram

Figure 2.6: Network Analyzer Test Configuration

Note that Figure 2.6(a) shows "Port 1" and "Port 2". These ports are not the detectors, only where the coaxial cable connects to the device. Calibration will adjust for all of the components up to the calibration planes, notated as "Cal 1 and Cal 2" in Figure 2.6(b). The electrical path from a detector to a calibration plane (Figure 2.6(b)) is known as the error adapter [19]. There are two error adapters that will need to be represented, "A" and "B" for reference here. The block "S" is the sample.

The system can be represented by the matrix equation,

$$\mathbf{T}^{ms} = \mathbf{T}^{A}\mathbf{T}^{S}\mathbf{T}^{B} \tag{2.25}$$

where the superscript ms is the detector measured value, A, B and S are represent the blocks from Figure 2.6(b). The $\mathbf{T}$ matrix can be related to the S-parameters by

$$\mathbf{T} = \frac{1}{S_{21}}\begin{bmatrix} S_{21}S_{12} - S_{11}S_{22} & S_{11} \\ -S_{22} & 1 \end{bmatrix}. \tag{2.26}$$

Rewriting (2.25) in terms of (2.26) and using superscripts to describe each block,

$$\mathbf{T}^{ms} = \frac{1}{S_{21}^{A}}\underbrace{\begin{bmatrix} S_{21}^{A}S_{12}^{A} - S_{11}^{A}S_{22}^{A} & S_{11}^{A} \\ -S_{22}^{A} & 1 \end{bmatrix}}_{\widetilde{\mathbf{T}}^{A}}\mathbf{T}^{S}\frac{1}{S_{21}^{B}}\underbrace{\begin{bmatrix} S_{21}^{B}S_{12}^{B} - S_{11}^{B}S_{22}^{B} & S_{11}^{B} \\ -S_{22}^{B} & 1 \end{bmatrix}}_{\widetilde{\mathbf{T}}^{B}} \tag{2.27}$$

Rearranging and identifying the unknowns,

$$\mathbf{T}^{ms} = \mathbf{T}^{S}\frac{1}{\boxed{S_{21}^{A}S_{21}^{B}}}\underbrace{\begin{bmatrix} \boxed{S_{21}^{A}S_{12}^{A}} - S_{11}^{A}S_{22}^{A} & \boxed{S_{11}^{A}} \\ -\boxed{S_{22}^{A}} & 1 \end{bmatrix}}_{\widetilde{\mathbf{T}}^{A}}\underbrace{\begin{bmatrix} \boxed{S_{21}^{B}S_{12}^{B}} - S_{11}^{B}S_{22}^{B} & \boxed{S_{11}^{B}} \\ -\boxed{S_{22}^{B}} & 1 \end{bmatrix}}_{\widetilde{\mathbf{T}}^{B}} \tag{2.28}$$

it is shown that there are seven unknown values to solve for: $S_{21}^{A}S_{21}^{B}$, $S_{21}^{A}S_{12}^{A}$, $S_{21}^{B}S_{12}^{B}$, S_{11}^{A}, S_{11}^{B}, S_{22}^{A}, and S_{22}^{B}.

2.8.1 TRL Calibration.

Now that the seven unknowns are identified, solutions can be derived. It is necessary to perform three calibration measurements to find solutions. The first is the "Thru"

(Figure 2.7(a)) measurement which is comprised of only the two waveguides being coupled together. The second is the "Reflect" measurement which involves placing a solid metal block on the end of each guide, where the calibration planes are located. The reflect measurement is shown in Figure 2.7(b) with two reflection standards placed between the waveguides, thus electrically terminating each guide. The final calibration measurement is the "Line" (Figure 2.7(c)) which requires the placement of a line standard (also known as the sample holder) in between the waveguides. In addition to recording the S-parameter values for each of these measurements, the "port mis-match" terms will also be collected from the NWA. These terms quantify the amount of power collected from each port reflecting from the opposite port and are displayed as a ratio.
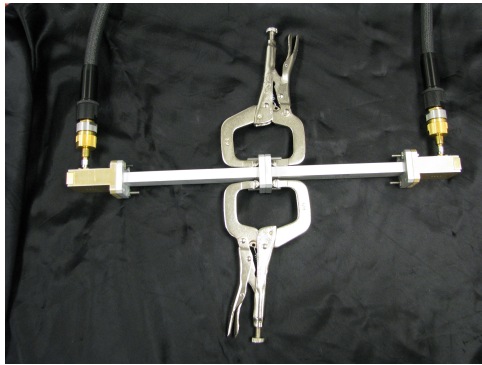
(a) Thru
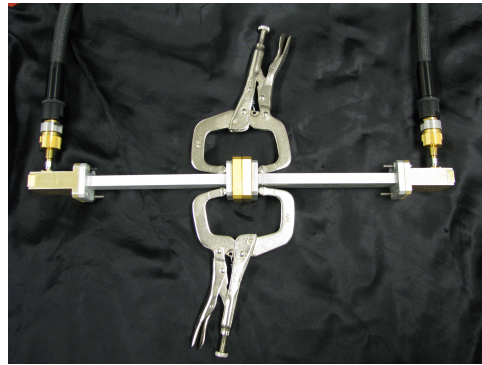
(b) Reflect
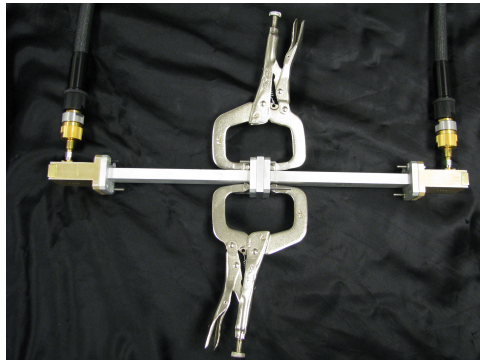
(c) Line

Figure 2.7: TRL Calibration Standard Configurations

2.8.1.1   Thru Measurement.

Writing (2.28) using superscripts to indicate the "Thru" measurement and utilizing the short hand indicated,

$$\mathbf{T}^{mt} = \frac{1}{S_{21}^{A} S_{21}^{B}} \widetilde{\mathbf{T}}^{A} \mathbf{T}^{t} \widetilde{\mathbf{T}}^{B}, \tag{2.29}$$

results in a matrix equation. Here, the focus is the $\mathbf{T}^{t}$ term. For a perfect waveguide, there should be no reflection and all the energy will be transmitted. Written mathematically,

$$S_{11}^{t}, S_{22}^{t} = 0 \tag{2.30}$$

$$S_{21}^{t}, S_{12}^{t} = 1. \tag{2.31}$$

Therefore, the value of the $\mathbf{T}^{t}$ term will be the identity matrix. This allows for solutions to the terms contained in the matrix,

$$\mathbf{T}^{t} = \frac{1}{S_{21}^{t}} \begin{bmatrix} S_{21}^{t} S_{12}^{t} - S_{11}^{t} S_{22}^{t} & S_{11}^{t} \\ -S_{22}^{t} & 1 \end{bmatrix} = \begin{bmatrix} 1 & 0 \\ 0 & 1 \end{bmatrix}. \tag{2.32}$$

The two terms with the tilde over them are unknowns that can be solved for using the Thru-Reflect-Line (TRL) measurements, after the common coefficient is factored out. Solving (2.29) for $\widetilde{T}^{B}$ yields,

$$\widetilde{\mathbf{T}}^{B} = \widetilde{\mathbf{T}}^{A^{-1}} \mathbf{T}^{mt} S_{21}^{A} S_{21}^{B}. \tag{2.33}$$

Now that an equation has been derived for one of the common tilde denoted terms, the derivation will proceed to the "Line" measurement.

2.8.1.2   Line Measurement.

In addition to physically holding the test sample, the line standard also serves to have a standard phase measurement. The standard itself is simply a short section of waveguide that aligns well to the rest of the system. Applying the same notation as in section 2.8.1.1 for the line measurement,

$$\mathbf{T}^{ml} = \frac{1}{S_{21}^{A} S_{21}^{B}} \widetilde{\mathbf{T}}^{A} \mathbf{T}^{l} \widetilde{\mathbf{T}}^{B}. \tag{2.34}$$

(a) Rectangular Standards: Line (L) and Reflect (R)

(b) DRWG Standards: Line (L) and Reflect (R)

Figure 2.8: Waveguide Standards

For a perfectly-aligned line standard, the S-parameters associated with reflection will be zero and the transmission parameters will simply undergo a phase change. Mathematically, this can be written as

$$S_{11}^l, S_{22}^l = 0 \tag{2.35}$$

$$S_{21}^l, S_{12}^l = e^{-jk_z l} = P, \tag{2.36}$$

where the l in the exponential is the length of the line standard, P is used for simplicity when re-writing, and k_z is wavenumber associated with the propagating wave in the z-direction (down the guide). Following the same procedure as section 2.8.1.1, $\mathbf{T}^l$ can be written as

$$\mathbf{T}^l = \frac{1}{P} \begin{bmatrix} P^2 & 0 \\ 0 & 1 \end{bmatrix} = \begin{bmatrix} P & 0 \\ 0 & P^{-1} \end{bmatrix}. \tag{2.37}$$

Substituting (2.33) into (2.34) yields,

$$\mathbf{T}^{ml} = \widetilde{\mathbf{T}}^A \mathbf{T}^l \widetilde{\mathbf{T}}^{A^{-1}} \mathbf{T}^{mt}. \tag{2.38}$$

By rearranging the terms in (2.38), another variable can be introduced to aid in solving the matrix equation. This is shown by

$$\underbrace{\mathbf{T}^{ml} \mathbf{T}^{mt^{-1}}}_{\mathbf{M}} = \widetilde{\mathbf{T}}^A \mathbf{T}^l \widetilde{\mathbf{T}}^{A^{-1}}, \tag{2.39}$$

22

where $\mathbf{M}$ is a matrix representing the product of $\mathbf{T}^{ml}$ and $\mathbf{T}^{mt^{-1}}$. Rearranging terms again to eliminate the inverse matrices produces

$$\mathbf{M}\widetilde{\mathbf{T}}^A = \widetilde{\mathbf{T}}^A\mathbf{T}^l. \tag{2.40}$$

Writing (2.40) in matrix form and substituting in (2.37) produces

$$\begin{bmatrix} m_{11} & m_{12} \\ m_{21} & m_{22} \end{bmatrix} \begin{bmatrix} \widetilde{A}_{11} & \widetilde{A}_{12} \\ \widetilde{A}_{21} & \widetilde{A}_{22} \end{bmatrix} = \begin{bmatrix} \widetilde{A}_{11} & \widetilde{A}_{12} \\ \widetilde{A}_{21} & \widetilde{A}_{22} \end{bmatrix} \begin{bmatrix} P & 0 \\ 0 & P^{-1} \end{bmatrix}, \tag{2.41}$$

where the m and $\widetilde{A}$ entries are elements of $\mathbf{M}$ and $\widetilde{\mathbf{T}}^A$ matrices respectively. By performing matrix multiplication on (2.41) produces four equations:

$$m_{11}\widetilde{A}_{11} + m_{12}\widetilde{A}_{21} = P\widetilde{A}_{11} \tag{2.42}$$

$$m_{21}\widetilde{A}_{11} + m_{22}\widetilde{A}_{21} = P\widetilde{A}_{21} \tag{2.43}$$

$$m_{11}\widetilde{A}_{12} + m_{12}\widetilde{A}_{22} = P^{-1}\widetilde{A}_{12} \tag{2.44}$$

$$m_{21}\widetilde{A}_{12} + m_{22}\widetilde{A}_{22} = P^{-1}\widetilde{A}_{22}. \tag{2.45}$$

Since there is a common term (P) in the first two equations, the next step will be to write one of them begin equivalent to P so it can be substituted in. Rearranging (2.43) results in,

$$m_{21}\frac{\widetilde{A}_{11}}{\widetilde{A}_{21}} + m_{22} = P. \tag{2.46}$$

Substitution of eq (2.46) into eq (2.42)

$$m_{11}\widetilde{A}_{11} + m_{12}\widetilde{A}_{21} = \left(m_{21}\frac{\widetilde{A}_{11}}{\widetilde{A}_{21}} + m_{21}\right)\widetilde{A}_{11}, \tag{2.47}$$

yields an equation that resembles a quadratic. Dividing (2.47) through by $\widetilde{A}_{21}$ and rearranging provides a quadratic equation:

$$m_{21}\left(\frac{\widetilde{A}_{11}}{\widetilde{A}_{21}}\right)^2 + (m_{22} - m_{11})\frac{\widetilde{A}_{11}}{\widetilde{A}_{21}} - m_{12} = 0. \tag{2.48}$$

23

Following the same process, but for (2.44) and (2.45), produces a second quadratic equation:

$$m_{21}\left(\frac{\widetilde{A}_{12}}{\widetilde{A}_{22}}\right)^2 + (m_{22} - m_{11})\frac{\widetilde{A}_{12}}{\widetilde{A}_{22}} - m_{12} = 0. \tag{2.49}$$

Equations (2.48) and (2.49) both satisfy the same form using the quadratic formula,

$$\frac{\widetilde{A}_{11}}{\widetilde{A}_{21}}, \frac{\widetilde{A}_{12}}{\widetilde{A}_{22}} = \frac{-(m_{22} - m_{11}) \pm \sqrt{(m_{22} - m_{11})^2 + 4m_{21}m_{12}}}{2m_{21}}. \tag{2.50}$$

Applying the matrix entries that constitute $\widetilde{A}_{11}$, $\widetilde{A}_{21}$, $\widetilde{A}_{12}$, and $\widetilde{A}_{22}$,

$$\frac{\widetilde{A}_{11}}{\widetilde{A}_{21}} = \frac{S_{21}^A S_{12}^A - S_{11}^A S_{22}^A}{-S_{22}^A} = S_{11}^A - \frac{S_{21}^A S_{12}^A}{S_{22}^A} = a \tag{2.51}$$

$$\frac{\widetilde{A}_{12}}{\widetilde{A}_{22}} = \frac{S_{11}^A}{1} = S_{11}^A = b \tag{2.52}$$

where a and b are used for simplicity in rewriting. For a typical network analyzer, the reflections should be low since there is just an empty guide, so the terms in (2.51) can be related using an inequality,

$$\left|S_{11}^A\right| << \left|\frac{S_{21}^A S_{12}^A}{S_{22}^A}\right|. \tag{2.53}$$

Using this information, it is determined that b is the small root and a is the large root of eq (2.50). By subtracting b from a and simplifying,

$$b - a = S_{11}^A - \left(S_{11}^A - \frac{S_{21}^A S_{12}^A}{S_{22}^A}\right) = \frac{S_{21}^A S_{12}^A}{S_{22}^A} \tag{2.54}$$

and rearranging for one of the seven unknowns mentioned previously,

$$S_{21}^A S_{12}^A = S_{22}^A (b - a). \tag{2.55}$$

At this point, expressions have been found for two of the seven unknowns. Now it will be necessary to revisit the thru and line measurement expressions again, but for different terms.

2.8.1.3 Recalculations of Thru and Line Expressions.

Using (2.29) and (2.32) and rearranging to solve in terms of $\widetilde{\mathbf{T}}^B$ will provide more equations. By making some observations about the variables, more independent equations can be realized. Solving for $\widetilde{\mathbf{T}}^A$ will yield

$$\widetilde{\mathbf{T}}^A = \mathbf{T}^{mt}\widetilde{\mathbf{T}}^{B^{-1}} S_{21}^A S_{21}^B. \tag{2.56}$$

Following the same process shown above (section 2.8.1.2), a matrix expression can be written as

$$\underbrace{\mathbf{T}^{mt^{-1}}\mathbf{T}^{ml}}_{\mathbf{N}} = \widetilde{\mathbf{T}}^{B^{-1}}\mathbf{T}^l\widetilde{\mathbf{T}}^B, \tag{2.57}$$

where $\mathbf{N}$ is shorthand for the product $\mathbf{T}^{mt^{-1}}\mathbf{T}^{ml}$. Rearranging and writing (2.57) to eliminate the inverse matrix produces,

$$\widetilde{\mathbf{T}}^B\mathbf{N} = \mathbf{T}^l\widetilde{\mathbf{T}}^B. \tag{2.58}$$

Since individual expressions are desired, the next step is to rewrite in matrix terms so multiplication can be used;

$$\begin{bmatrix} \widetilde{B}_{11} & \widetilde{B}_{12} \\ \widetilde{B}_{21} & \widetilde{B}_{22} \end{bmatrix} \begin{bmatrix} n_{11} & n_{12} \\ n_{21} & n_{22} \end{bmatrix} = \begin{bmatrix} P & 0 \\ 0 & P^{-1} \end{bmatrix} \begin{bmatrix} \widetilde{B}_{11} & \widetilde{B}_{12} \\ \widetilde{B}_{21} & \widetilde{B}_{22} \end{bmatrix}. \tag{2.59}$$

Again, explicitly writing out the matrix multiplication operation will produce four equations:

$$\widetilde{B}_{11}n_{11} + \widetilde{B}_{12}n_{21} = P\widetilde{B}_{11} \tag{2.60}$$

$$\widetilde{B}_{11}n_{12} + \widetilde{B}_{12}n_{22} = P\widetilde{B}_{12} \tag{2.61}$$

$$\widetilde{B}_{21}n_{11} + \widetilde{B}_{22}n_{21} = P^{-1}\widetilde{B}_{21} \tag{2.62}$$

$$\widetilde{B}_{21}n_{12} + \widetilde{B}_{22}n_{22} = P^{-1}\widetilde{B}_{22}. \tag{2.63}$$

Solving (2.61) for P,

$$\frac{\widetilde{B}_{11}}{\widetilde{B}_{12}}n_{12} + n_{22} = P, \tag{2.64}$$

and substitution into (2.60) gives,

$$\widetilde{B}_{11} n_{11} + \widetilde{B}_{12} n_{21} = \left(\frac{\widetilde{B}_{11}}{\widetilde{B}_{12}} + n_{22} \right) \widetilde{B}_{11}. \tag{2.65}$$

Rearranging and dividing by $\widetilde{B}_{12}$ results in,

$$\left(\frac{\widetilde{B}_{11}}{\widetilde{B}_{12}} \right)^2 n_{12} + (n_{22} - n_{11}) \frac{\widetilde{B}_{11}}{\widetilde{B}_{12}} - n_{21} = 0. \tag{2.66}$$

Using the same procedure, but for (2.62) and (2.63), another equation of similar form as (2.66) is formed,

$$\left(\frac{\widetilde{B}_{21}}{\widetilde{B}_{22}} \right)^2 n_{12} + (n_{22} - n_{11}) \frac{\widetilde{B}_{21}}{\widetilde{B}_{22}} - n_{21} = 0. \tag{2.67}$$

Finally, a quadratic equation similar to (2.50) is realized,

$$\frac{\widetilde{B}_{11}}{\widetilde{B}_{11}}, \frac{\widetilde{B}_{21}}{\widetilde{B}_{22}} = \frac{-(n_{22} - n_{11}) \pm \sqrt{(n_{22} - n_{11})^2 + 4n_{21}n_{12}}}{2n_{12}}. \tag{2.68}$$

Showing the two solutions as products of their constitutive S-parameters,

$$\frac{\widetilde{B}_{11}}{\widetilde{B}_{12}} = \frac{S_{21}^B S_{12}^B - S_{11}^B S_{22}^B}{S_{22}^B} = -S_{22}^B - \frac{S_{21}^B S_{12}^B}{S_{11}^B} = c \tag{2.69}$$

$$\frac{\widetilde{B}_{21}}{\widetilde{B}_{22}} = \frac{-S_{22}^B}{1} = -S_{22}^B = d, \tag{2.70}$$

where two more variables, c and d, are used for simplicity in rewriting. Again, using the fact that a typical NWA will have low reflection,

$$\left| -S_{22}^B \right| << \left| \frac{S_{21}^B S_{12}^B}{S_{22}^B} \right|. \tag{2.71}$$

So, c will be the large root and d will be the small root of (2.68). Subtracting d from c and rearranging will yield a solution for another of the seven original unknowns

$$S_{21}^B S_{12}^B = S_{11}^B (c - d). \tag{2.72}$$

Four of the original seven unknowns have been found. Additional measurement expressions will be required to find the remaining terms.

2.8.1.4 Reflect Terms.

The reflect standard can be shown mathematically from Port 1 as [19],

$$S_{11}^{mr} = S_{11}^{A} + \frac{S_{21}^{A} S_{12}^{A} \Gamma^{r}}{1 - S_{22}^{A} \Gamma^{r}}. \tag{2.73}$$

Solving for Γ^{r} yields

$$\Gamma^{r} = \frac{\left(S_{11}^{mr} - S_{11}^{A} \right)}{\left(S_{21}^{A} S_{12}^{A} + \left(S_{11}^{mr} - S_{11}^{A} \right) S_{22}^{A} \right)}, \tag{2.74}$$

where the superscript *mr* signifies the measured reflect terms. Substituting in the variables already defined, a and b, (2.74) can be written as,

$$\Gamma^{r} = \frac{S_{11}^{mr} - b}{S_{22}^{A} \left(S_{11}^{mr} - a \right)}. \tag{2.75}$$

For a short that is placed with no offset from the end of the waveguide, the value of Γ^{r} should be extremely close to -1, indicative of a strong reflection. Applying similar steps starting at (2.73) for the reflect parameter from Port 2,

$$S_{22}^{mr} = S_{22}^{B} + \frac{S_{12}^{B} S_{21}^{B} \Gamma^{r}}{1 - S_{11}^{B} \Gamma^{r}} \tag{2.76}$$

and substituting in c and d,

$$\Gamma^{r} = \frac{S_{22}^{mr} + d}{S_{11}^{B} \left(S_{22}^{mr} + c \right)}, \tag{2.77}$$

will result in a similar equation to (2.77). Setting (2.75) equal to (2.77),

$$\frac{S_{11}^{mr} - b}{S_{22}^{A} \left(S_{11}^{mr} - a \right)} = \frac{S_{22}^{mr} + d}{S_{11}^{B} \left(S_{22}^{mr} + c \right)} \tag{2.78}$$

and solving for S_{22}^{A} yields

$$S_{22}^{A} = S_{11}^{B} \frac{\left(S_{22}^{mr} + c \right) \left(S_{11}^{mr} - b \right)}{\left(S_{22}^{mr} + d \right) \left(S_{11}^{mr} - a \right)}. \tag{2.79}$$

Five of the seven unknowns now have expressions. For the final two, a revisit of the thru expressions will have to occur. The following expressions assume that there is no detector

mis-match. This is not true for a real NWA, so later on correction for the mis-match will be derived. If the detector mis-match has been corrected, then

$$S_{11}^{mt} = S_{11}^{A} + \frac{S_{21}^{A} S_{12}^{A} S_{11}^{B}}{1 - S_{22}^{A} S_{11}^{B}}. \tag{2.80}$$

Solving for S_{11}^{B} and substituting in a and b gives,

$$S_{11}^{B} = \frac{S_{11}^{mt} - b}{S_{22}^{A} \left(S_{11}^{mt} - a \right)}, \tag{2.81}$$

which is the sixth unknown. Applying (2.81) to (2.79) provides an expression for S_{22}^{A}:

$$S_{22}^{A} = \frac{\left(S_{11}^{mt} - b \right)}{S_{22}^{A} \left(S_{11}^{mt} - a \right)} \frac{\left(S_{22}^{mr} + c \right) \left(S_{11}^{mr} - b \right)}{\left(S_{22}^{mr} + d \right) \left(S_{11}^{mr} - a \right)}. \tag{2.82}$$

Multiplying both sides of the equation by S_{22}^{A} and taking the square root of the entire expression results in

$$S_{22}^{A} = \pm \left[\frac{\left(S_{11}^{mt} - b \right) \left(S_{11}^{mr} - b \right) \left(S_{22}^{mr} + c \right)}{\left(S_{11}^{mt} - a \right) \left(S_{11}^{mr} - a \right) \left(S_{22}^{mr} + d \right)} \right]^{1/2}, \tag{2.83}$$

and a root choice is required. Using (2.75) and the fact that, for a reflect standard $\Gamma^{r} \approx -1 + 0j$, the real part of Γ^{r} should be less than zero. To use this information, each root of S_{22}^{A} will have to be substituted into (2.75) and the appropriate root chosen. To find the seventh and final unknown, the S_{21}^{mt} will be revisited to provide an additional expression. Solving

$$S_{21}^{mt} = \frac{S_{21}^{A} S_{21}^{A}}{1 - S_{22}^{A} S_{11}^{B}}, \tag{2.84}$$

and rearranging for the final unknown shows,

$$S_{21}^{A} S_{21}^{B} = S_{21}^{mt} \left(1 - S_{22}^{A} S_{11}^{B} \right). \tag{2.85}$$

Now all of the unknowns have been found, but the port mis-match problem has not yet been addressed.

28

2.8.1.5 Port Mis-match Correction.

From Rytting [19], the source and load mismatch terms can be determined from the following matrix equation:

$$\begin{bmatrix} b_{1m} & b'_{1m} \\ b_{2m} & b'_{2m} \end{bmatrix} = \begin{bmatrix} S^m_{11} & S^m_{12} \\ S^m_{21} & S^m_{22} \end{bmatrix} \begin{bmatrix} a_{1m} & a'_{1m} \\ a_{2m} & a'_{2m} \end{bmatrix} \tag{2.86}$$

Rearranging to solve for S^m terms,

$$\begin{bmatrix} S^m_{11} & S^m_{12} \\ S^m_{21} & S^m_{22} \end{bmatrix} = \begin{bmatrix} b_{1m} & b'_{1m} \\ b_{2m} & b'_{2m} \end{bmatrix} \frac{1}{a_{1m}a'_{2m} - a'_{1m}a_{2m}} \begin{bmatrix} a'_{2m} & -a'_{1m} \\ -a_{2m} & a'_{1m} \end{bmatrix}. \tag{2.87}$$

Performing matrix multiplication and simplifying,

$$S^m_{11} = \frac{S^d_{11} - S^d_{12}\frac{a_{2m}}{a_{1m}}}{1 - \frac{a_{2m}}{a_{1m}}\frac{a'_{1m}}{a'_{2m}}} \tag{2.88}$$

$$S^m_{12} = \frac{S^d_{12} - S^d_{11}\frac{a'_{1m}}{a'_{2m}}}{1 - \frac{a_{2m}}{a_{1m}}\frac{a'_{1m}}{a'_{2m}}} \tag{2.89}$$

$$S^m_{21} = \frac{S^d_{21} - S^d_{22}\frac{a_{2m}}{a_{1m}}}{1 - \frac{a_{2m}}{a_{1m}}\frac{a'_{1m}}{a'_{2m}}} \tag{2.90}$$

$$S^m_{22} = \frac{S^d_{22} - S^d_{21}\frac{a'_{1m}}{a'_{2m}}}{1 - \frac{a_{2m}}{a_{1m}}\frac{a'_{1m}}{a'_{2m}}} \tag{2.91}$$

where the superscript d indicates the detector measurement. The a and b terms are available as additional output from the NWA, displayed as ratios, $R2/R1$ and $R1/R2$. The measurements correspond to the equations above by,

$$\text{Port 1,} \frac{R2}{R1} = \frac{a_{2m}}{a_{1m}} \tag{2.92}$$

$$\text{Port 2,} \frac{R1}{R2} = \frac{a'_{1m}}{a'_{2m}} \tag{2.93}$$

All the terms necessary to correct for port mis-match have been found and the TRL calibration scheme is complete.

29

III. Methodology

T HE previous chapter demonstrated the algorithms and mathematics required to understand a NWA based measurement system. The equipment configuration using DRWG and data acquired will appear similar to those of rectangular waveguide. Calibration will be accomplished in MATLAB using the four measurements detailed below. The final step is to derive the constitutive parameters using the NRW algorithm [17, 21].

3.1 Double Ridged Waveguide Analysis

To make the analysis of the DRWG tractable, the geometry can be broken down into three regions and the common coordinate system will be located in the center of the guide, as shown in Figure 3.1 [12]. The point at the upper right corner of region I will be considered $(\Delta x, \Delta y)$. The point located at the upper right of region II is referred to as $\left(\frac{a}{2}, \frac{b}{2}\right)$.

The first step for this analysis will be to define the fields using the vector potentials, $\mathbf{F}$ and $\mathbf{A}$. Since the coordinate system has been chosen to have the z direction as the waveguide axis and an electric source is assumed ($\mathbf{TE^z}$),

$$\mathbf{F} = \hat{z}F_z \tag{3.1}$$

$$\mathbf{A} = 0. \tag{3.2}$$

The forcing function for the propagating wave in the z direction is given by

$$F_z = \underbrace{(B\cos k_x x + C\sin k_x x)}_{f(x)}\underbrace{(D\cos k_y y + E\sin k_y y)}_{g(y)}\underbrace{(A^+ e^{-jk_z z} + A^- e^{jk_z z})}_{h^+(z)} \tag{3.3}$$

where A,B,C,D and E are constants and k is the wavenumber in a given direction. For simplicity and conciseness, the terms $f(x)$, $g(y)$ and $h^+(z)$ will be used in place of the terms in (3.3). The electric field intensity ($\mathbf{E}$) and the magnetic field intensity ($\mathbf{H}$) can be expressed as

$$\mathbf{E} = \frac{1}{j\omega\epsilon\mu}\left[k^2\mathbf{A} + \nabla(\nabla \cdot \mathbf{A})\right] - \frac{\nabla \times \mathbf{F}}{\epsilon} \tag{3.4}$$

30

$$\mathbf{H} = \frac{\nabla \times \mathbf{A}}{\mu} + \frac{1}{j\omega\epsilon\mu}\left[k^2\mathbf{F} + \nabla(\nabla \cdot \mathbf{F})\right]. \tag{3.5}$$

Applying (3.1) and (3.72) into (3.4) and (3.5) yields

$$\mathbf{E} = -\frac{\nabla \times \mathbf{F}}{\epsilon} \tag{3.6}$$

$$\mathbf{H} = \frac{1}{j\omega\epsilon\mu}\left[k^2\mathbf{F} + \nabla(\nabla \cdot \mathbf{F})\right]. \tag{3.7}$$

To continue, each field vector will need to be broken up into its respective field components. This is accomplished by performing the operations in (3.6) and (3.7). The field components are:

$$E_x = \frac{k_y}{\epsilon}f(x)(D\sin k_y y - E\cos k_y y)h^+(z) \tag{3.8}$$

$$E_y = -\frac{k_x}{\epsilon}(B\cos k_x x - C\sin k_x x)g(y)h^+(z) \tag{3.9}$$

$$E_z = 0 \tag{3.10}$$

$$H_x = \frac{k_x k_z}{j\omega\epsilon\mu}(B\sin k_x x - C\cos k_x x)g(y)\underbrace{(A^+e^{-jk_z z} - A^-e^{jk_z z})}_{h^-(z)} \tag{3.11}$$

$$H_y = \frac{k_y k_z}{j\omega\epsilon\mu}f(x)(D\sin k_y y - E\cos k_y y)h^-(z) \tag{3.12}$$

$$H_z = \frac{1}{j\omega\epsilon\mu}\underbrace{(k^2 + k_z^2)}_{k_c^2}F_z \tag{3.13}$$

$$= \frac{k_c^2}{j\omega\epsilon\mu}f(x)g(y)h^+(z) \tag{3.14}$$

where k_c is the cutoff wavenumber of the guide. Now that the general fields have been derived, analysis can continue by deriving the terms for each region. Since the boundary conditions for each region will vary from each other, each region will be derived separately and the coordinate system will have an origin at the center of the guide. The configurations for analysis are shown in Figure 3.1.

3.1.1 Region I.

Region I contains a PEC at the top and bottom boundaries which are located at $\pm\Delta y$. This region is also called the "gap" region. Since the origin of the coordinate system is
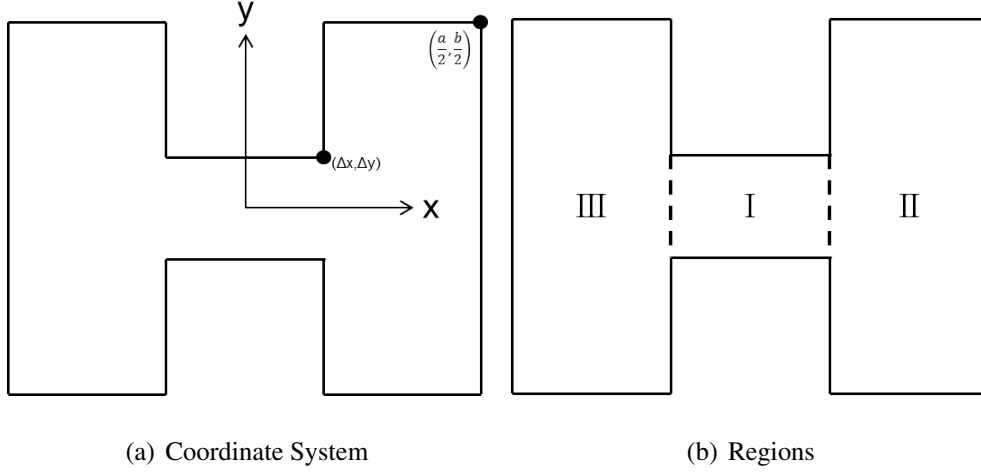
31

(a) Coordinate System   (b) Regions

Figure 3.1: DRWG Configurations for Analysis

chosen to be at the center of the guide, there will be a "shift" term substituted in for the variables in each term. For region I, the field equations shown generically in (3.8)-(3.14) can be written as:

$$E_{x_1} = \frac{k_y}{\epsilon} f(x)(D \sin k_y(y - \Delta y) - E \cos k_y(y - \Delta y))h^+(z) \tag{3.15}$$

$$E_{y_1} = -\frac{k_x}{\epsilon}(B \cos k_x x - C \sin k_x x)g(y - \Delta y)h^+(z) \tag{3.16}$$

$$E_{z_1} = 0 \tag{3.17}$$

$$H_{x_1} = \frac{k_x k_z}{j\omega\epsilon\mu}(B \sin k_x x - C \cos k_x x)g(y - \Delta y)h^-(z) \tag{3.18}$$

$$H_{y_1} = \frac{k_y k_z}{j\omega\epsilon\mu} f(x)(D \sin k_y(y - \Delta y) - E \cos k_y(y - \Delta y))h^-(z) \tag{3.19}$$

$$H_{z_1} = \frac{1}{j\omega\epsilon\mu} \underbrace{(k^2 + k_z^2)}_{k_c^2} F_z \tag{3.20}$$

$$= \frac{k_c^2}{j\omega\epsilon\mu} f(x)g(y - \Delta y))h^+(z), \tag{3.21}$$

where $(y - \Delta y)$ has been substituted in for x. At the upper and lower PEC boundaries $(y = \pm \Delta y)$, the tangential electric fields will be zero. In this case, the x and z directed fields

32

will be zero and can be written as,

$$E_{x_1} \underset{\substack{y=\pm\Delta y \\ z=(-\infty,+\infty)}}{=} 0. \tag{3.22}$$

Applying the boundary condition to (3.15) will yield two equations:

$$E_{x_1}(y = \Delta y) = D_1 \sin k_{y_1}(0) - E_1 \cos k_{y_1}(0) = 0 \tag{3.23}$$

$$E_{x_1}(y = -\Delta y) = D_1 \sin k_{y_1}(-2\Delta y) = 0. \tag{3.24}$$

Solving the two equations will yield a result for one of the constants and for the y associated wavenumber:

$$E_1 = 0 \tag{3.25}$$

$$k_{y_1} = \frac{n\pi}{2\Delta y}. \tag{3.26}$$

Since there is no PEC boundary on the right or left side, more analysis will need to be done before applying a boundary condition to the fields there.

3.1.2   Region II.

This section will analyze region II as defined in Figure 3.1(b). This region will also be referred to as the "trough" region in later notation. Again, the assumption that the waveguide walls can be modeled as a PEC has been made. The forcing function will be of the same form as in the previous analysis and will have a different "shift" term associated with it. The function for region II is given by,

$$F_{z_2} = \underbrace{\left(B_2 \cos k_{x_2}\left(\frac{a}{2} - x\right) + C_2 \sin k_{x_2}\left(\frac{a}{2} - x\right)\right)}_{f_2(x)} \underbrace{\left(D_2 \cos k_{y_2}\left(y - \frac{b}{2}\right) + E_2 \sin k_{y_2}\left(y - \frac{b}{2}\right)\right)}_{g_2(y)} h^+(z)$$

$$\tag{3.27}$$

where $h^+(z)$ is the same as before and the subscript "2" signifies region II. The field equations are given by:

$$E_{x_2} = k_{y_2} f_2(x) \left(D_2 \sin k_{y_2} \left(y - \frac{b}{2} \right) - E_2 \cos k_{y_2} \left(y - \frac{b}{2} \right) \right) h^+(z) \tag{3.28}$$

$$E_{y_2} = -k_{x_2} \left(B_2 \sin k_{x_2} \left(\frac{a}{2} - x \right) - C_2 \cos k_{x_2} \left(\frac{a}{2} - x \right) \right) g_2(y) h^+(z) \tag{3.29}$$

$$E_{z_2} = 0 \tag{3.30}$$

$$H_{x_2} = \frac{k_{x_2} k_z}{j\omega\mu} \left(B_2 \sin k_{x_2} \left(\frac{a}{2} - x \right) - C_2 \cos k_{x_2} \left(\frac{a}{2} - x \right) \right) g_2(y) h^-(z) \tag{3.31}$$

$$H_{y_2} = \frac{k_{y_2} k_z}{j\omega\mu} f_2(x) \left(D_2 \sin k_{y_2} \left(y - \frac{b}{2} \right) - E_2 \cos k_{x_2} \left(y - \frac{b}{2} \right) \right) h^-(z) \tag{3.32}$$

$$H_{z_2} = \frac{k_c^2}{j\omega\mu} f_2(x) g_2(y) h^+(z) \tag{3.33}$$

where $h^-(z)$ is the same as in section 3.1.1. The PEC exists at the x value $\frac{a}{2}$, and y values $\pm\frac{b}{2}$, which can be written as

$$E_{x_2} \Big|_{\substack{y=\pm\frac{b}{2} \\ z=(-\infty,+\infty)}} = 0 \tag{3.34}$$

$$E_{y_2} \Big|_{\substack{y=\frac{a}{2} \\ z=(-\infty,+\infty)}} = 0. \tag{3.35}$$

Applying the PEC boundary conditions to the field equations results in

$$E_2 = 0 \tag{3.36}$$

$$C_2 = 0 \tag{3.37}$$

and

$$D_2 \sin k_{y_2}(b) = 0 \tag{3.38}$$

$$k_{y_2} = \frac{m\pi}{b}. \tag{3.39}$$

By inspection of Figure 3.1(b), region II and region III will be similar in analysis.

3.1.3 Region III.

The geometry of regions II and III will be similar, but the variables will differ due to different locations of the PEC boundary. Region III is also called a "trough" region. Again, starting with the forcing function, modified for region III,

$$F_{z_3} = \underbrace{\left(B_3 \cos k_{x_3}\left(\frac{a}{2} + x\right) + C_3 \sin k_{x_3}\left(\frac{a}{2} + x\right)\right)}_{f_3(x)}\underbrace{\left(D_3 \cos k_{y_3}\left(y - \frac{b}{2}\right) + E_3 \sin k_{y_3}\left(y - \frac{b}{2}\right)\right)}_{g_3(y)}h^+(z)$$

$$(3.40)$$

The field equations are given by:

$$E_{x_3} = k_{y_3} f_3(x)\left(D_3 \sin k_{y_3}\left(y - \frac{b}{2}\right) - E_3 \cos k_{y_3}\left(y - \frac{b}{2})\right)\right)h^+(z) \tag{3.41}$$

$$E_{y_3} = -k_{x_3}\left(B_3 \sin k_{x_3}\left(\frac{a}{2} + x\right) - C_3 \cos k_{x_3}\left(\frac{a}{2} + x)\right)\right)g_3(y)h^+(z) \tag{3.42}$$

$$E_{z_3} = 0 \tag{3.43}$$

$$H_{x_3} = \frac{k_{x_3}k_z}{j\omega\mu}\left(B_3 \sin k_{x_3}\left(\frac{a}{2} + x\right) - C_3 \cos k_{x_3}\left(\frac{a}{2} + x)\right)\right)g_3(y)h^-(z) \tag{3.44}$$

$$H_{y_3} = \frac{k_{y_3}k_z}{j\omega\mu}f_3(x)\left(D_3 \sin k_{y_3}\left(y - \frac{b}{2}\right) - E_3 \cos k_{x_3}\left(y - \frac{b}{2})\right)\right)h^-(z) \tag{3.45}$$

$$H_{z_3} = \frac{k_c^2}{j\omega\mu}f_3(x)g_3(y)h^+(z) \tag{3.46}$$

The boundaries are located at $y = \pm\frac{b}{2}$ and $x = -\frac{a}{2}$. Shown mathematically,

$$E_{x_3}\Big|_{\substack{y=\pm\frac{b}{2} \\ z=(-\infty,+\infty)}} = 0 \tag{3.47}$$

$$E_{y_3}\Big|_{\substack{y=-\frac{a}{2} \\ z=(-\infty,+\infty)}} = 0. \tag{3.48}$$

Applying the PEC boundary conditions to the field equations results in

$$E_3 = 0 \tag{3.49}$$

$$C_3 = 0 \tag{3.50}$$

and

$$D_3 \sin k_{y_3}(b) = 0 \tag{3.51}$$

$$k_{y_3} = \frac{m\pi}{b}. \tag{3.52}$$

Additionally, comparing the expressions for the wave numbers in regions II and III, the observation

$$k_{x_2} = k_{x_3} \tag{3.53}$$

can be made. Equation (3.53) will be useful in determining the rest of the unknown equations for this analysis.

3.1.4   *Continuous Fields Boundary Conditions.*

The final boundary condition to apply is the existence of continuous fields at the transitional line between each region. This region will be referred to as the "gap" boundary region. The boundary conditions require that the tangential electric and magnetic fields be continuous at this gap [15]. For this analysis, let

$$E_1(y') \text{ be the gap electric field at } x = \Delta x \tag{3.54}$$

$$E_2(y') \text{ be the gap electric field at } x = -\Delta x. \tag{3.55}$$

Writing the field expression and substituting in the values found in Sections 3.1.1 - 3.1.3, the expressions for $E_1(y')$ and $E_2(y')$ can be written as [15],

$$
\begin{aligned}
E_1(y') = -\sum_n k_{x_{1n}} \left(B_{1n} \sin k_{x_{1n}} x - C_{1n} \cos k_{x_{1n}} x \right) \cos\left(\frac{n\pi}{2\Delta y} (y' - \Delta y) \right) = \\
\sum_m k_{x_{2m}} B_{2m} \sin k_{x_{2m}} \left(\frac{a}{2} - \Delta x \right) \cos \frac{m\pi}{b} \left(y' - \frac{b}{2} \right)
\end{aligned}
\tag{3.56}
$$

$$
\begin{aligned}
E_2(y') = \sum_n k_{x_{1n}} \left(B_{1n} \sin k_{x_{1n}} x + C_{1n} \cos k_{x_{1n}} x \right) \cos\left(\frac{n\pi}{2\Delta y} (y' - \Delta y) \right) = \\
-\sum_m k_{x_{2m}} B_{3m} \sin k_{x_{2m}} \left(\frac{a}{2} - \Delta x \right) \cos \frac{m\pi}{b} \left(y' - \frac{b}{2} \right).
\end{aligned}
\tag{3.57}
$$

36

A series representation of the fields will be difficult to solve for the unknowns. Performing integration on the expression will "filter" the series to acquire the "nth" term. From the identity [13],

$$\int_{a-L}^{a+L} \cos\frac{m\pi x}{L} \cos\frac{n\pi x}{L} dx = \begin{cases} 0 & m \neq n \\ L & m = n \neq 0 \\ 2L & m = n = 0 \end{cases} \quad (3.58)$$

it can be observed that the series can be simplified by multiplication the original function (3.56) and integration over the boundary. Application of (3.58) yields the following two equations:

$$\int_{-\Delta y}^{\Delta y} E_1(y') \cos\frac{n\pi}{2\Delta y}(y' - \Delta y) dy' = -k_{x_{1n}}(B_{1n} \sin k_{x_{1n}}\Delta x - C_{1n} \cos k_{x_{1n}}\Delta x)\Delta y (1 + \delta_{n,0})$$

$$(3.59)$$

$$\int_{-\Delta y}^{\Delta y} E_1(y') \cos\frac{m\pi}{b}\left(y' - \frac{b}{2}\right) dy' = k_{x_{2m}} B_{2m} \sin k_{x_{2m}}\left(\frac{a}{2} - \Delta x\right)\frac{b}{2}(1 + \delta_{m,0}), \quad (3.60)$$

where the Kronecker Delta function facilitates the solution given in (3.58). Similar expressions involving $E_2(y')$ can be written,

$$\int_{-\Delta y}^{\Delta y} E_2(y') \cos\frac{n\pi}{2\Delta y}(y' - \Delta y) dy' = k_{x_{1n}}(B_{1n} \sin k_{x_{1n}}\Delta x + C_{1n} \cos k_{x_{1n}}\Delta x)\Delta y (1 + \delta_{n,0})$$

$$(3.61)$$

$$\int_{-\Delta y}^{\Delta y} E_2(y') \cos\frac{m\pi}{b}\left(y' - \frac{b}{2}\right) dy' = -k_{x_{2m}} B_{3m} \sin k_{x_{2m}}\left(\frac{a}{2} - \Delta x\right)\frac{b}{2}(1 + \delta_{m,0}). \quad (3.62)$$

Solving for B_{2m} and B_{3m} in (3.60) and (3.62) produces

$$B_{2m} = \frac{\int\limits_{-\Delta y}^{\Delta y} E_1(y') \cos \frac{m\pi}{b} \left(y' - \frac{b}{2}\right) dy'}{k_{x_{2m}} \frac{b}{2}(1 + \delta_{m,0}) \sin k_{x_{2m}} \left(\frac{a}{2} - \Delta x\right)} \tag{3.63}$$

$$B_{3m} = \frac{-\int\limits_{-\Delta y}^{\Delta y} E_2(y') \cos \frac{m\pi}{b} \left(y' - \frac{b}{2}\right) dy'}{k_{x_{2m}} \frac{b}{2}(1 + \delta_{m,0}) \sin k_{x_{2m}} \left(\frac{a}{2} - \Delta x\right)}. \tag{3.64}$$

$$\tag{3.65}$$

To simplify further analysis, the numerators in (3.63) and (3.64) will be referred to as I_3 and I_4 respectively. If (3.59) and (3.61) are rearranged to

$$C_{1n} \cos k_{x_{1n}} \Delta x - B_{1n} \sin k_{x_{1n}} \Delta x = \frac{\int\limits_{-\Delta y}^{\Delta y} E_1(y') \cos \frac{n\pi}{2\Delta y} \left(y' - \frac{b}{2}\right) dy'}{k_{x_{1n}} \Delta y \left(1 + \delta_{n,0}\right)} \tag{3.66}$$

$$C_{1n} \cos k_{x_{1n}} \Delta x + B_{1n} \sin k_{x_{1n}} \Delta x = \frac{\int\limits_{-\Delta y}^{\Delta y} E_2(y') \cos \frac{n\pi}{2\Delta y} \left(y' - \frac{b}{2}\right) dy'}{k_{x_{1n}} \Delta y \left(1 + \delta_{n,0}\right)}, \tag{3.67}$$

$$\tag{3.68}$$

it will be possible to solve for C_{1n} and B_{1n} with simple expressions if the same shorthand is used as before. The numerators of (3.66) and (3.67) will be referred to as I_1 and I_2 respectively. Now C_{1n} and B_{1n} can be written as

$$C_{1n} = \frac{I_1 + I_2}{2k_{x_{1n}} \Delta y \left(1 + \delta_{n,0}\right) \cos k_{x_{1n}} \Delta x} \tag{3.69}$$

$$B_{1n} = \frac{I_2 - I_1}{2k_{x_{1n}} \Delta y \left(1 + \delta_{n,0}\right) \sin k_{x_{1n}} \Delta x}. \tag{3.70}$$

Now that these constants have been found, (3.56) and (3.57) can be written by substituting in the values found in (3.69) and (3.70). The gap magnetic fields must by continuous by the boundary condition [15], so equating the tangential magnetic field at the boundary will produce continuity. For this analysis, the z-directed fields will be used. Selecting the field

in region I and equating it to the field in region II at the gap,

$$H_{z1}(x = -\Delta x) = H_{z2}(x = -\Delta x), \tag{3.71}$$

the following expression is formed after substitution of the shorthand and constants previously solved for:

$$\sum_n \frac{I_1\left(\tan k_{x_{1n}}\Delta x - \cot k_{x_{1n}}\Delta x\right) + I_2\left(\tan k_{x_{1n}}\Delta x + \cot k_{x_{1n}}\Delta x\right)}{2k_{x_{1n}}\Delta y\left(1 + \delta_{n,0}\right)} \cos \frac{n\pi}{2\Delta y}(y - \Delta y) -$$

$$\sum_m \frac{I_3 \cot k_{x_{2m}}\left(\frac{a}{2} - \Delta x\right)}{k_{x_{2m}}\frac{b}{2}\left(1 + \delta_{m,0}\right)} \cos \frac{m\pi}{b}\left(y - \frac{b}{2}\right) = 0. \tag{3.72}$$

Applying the same technique and boundary condition to the gap field between region I and region III,

$$H_{z1}(x = -\Delta x) = H_{z3}(x = -\Delta x), \tag{3.73}$$

a similar expression as (3.72) will arise:

$$\sum_n \frac{I_1\left(\tan k_{x_{1n}}\Delta x + \cot k_{x_{1n}}\Delta x\right) + I_2\left(\tan k_{x_{1n}}\Delta x - \cot k_{x_{1n}}\Delta x\right)}{2k_{x_{1n}}\Delta y\left(1 + \delta_{n,0}\right)} \cos \frac{n\pi}{2\Delta y}(y - \Delta y) -$$

$$\sum_m \frac{I_4 \cot k_{x_{2m}}\left(\frac{a}{2} - \Delta x\right)}{k_{x_{2m}}\frac{b}{2}\left(1 + \delta_{m,0}\right)} \cos \frac{m\pi}{b}\left(y - \frac{b}{2}\right) = 0. \tag{3.74}$$

Since the goal for this analysis is to obtain the cutoff frequency for use in later calculations, solving for the wavenumbers will be critical.

3.1.5 Finding the Cutoff Frequency.

As stated, the primary purpose of this analysis for this work is to find the cutoff wavenumber. For the DRWG geometry, the cutoff wavenumber can be related to the other wavenumbers associated with each region by,

$$k_c^2 = k_{yg}^2 + k_{xg}^2 \tag{3.75}$$

$$k_c^2 = k_{yt}^2 + k_{xt}^2 \tag{3.76}$$

where k_c is the cutoff wavenumber, and the subscripts g and t indicate the gap and trough modes [15]. The cutoff wavenumber for this system is the point when k_z is zero, so

39

generation of equations that will result in zero for k_z is important. To do this, $E_1(y')$, $E_2(y')$, I_1, I_2, I_3 and I_4 will be rearranged and the unknown modal amplitudes (α and β) will be substituted in,

$$E_1(y') = \sum_l \alpha_l \cos\left(\frac{l\pi}{2\Delta y}\right)(y' - \Delta y) \tag{3.77}$$

$$E_2(y') = \sum_l \beta_l \cos\left(\frac{l\pi}{2\Delta y}\right)(y' - \Delta y) \tag{3.78}$$

$$I_1 = \sum_l \alpha_l \Delta y\, (1 + \delta_{l,0})\, \delta_{l,n} \tag{3.79}$$

$$I_2 = \sum_l \beta_l \Delta y\, (1 + \delta_{l,0})\, \delta_{l,n} \tag{3.80}$$

$$I_3 = \sum_l \alpha_l \psi^+(m, l) \tag{3.81}$$

$$I_4 = \sum_l \beta_l \psi^+(m, l) \tag{3.82}$$

where

$$\psi^+(m, l) = \frac{1}{2}\left(\frac{1}{k_{y_{1n}} - k_{y_{2n}}} - \frac{1}{k_{y_{1n}} + k_{y_{2n}}}\right)\left[\sin\left(m\pi\left(\frac{1}{2} - \frac{\Delta y}{b}\right)\right) - (-1)^n \sin\left(m\pi\left(\frac{1}{2} + \frac{\Delta y}{b}\right)\right)\right]. \tag{3.83}$$

To continue the analysis, the testing function is

$$\int_{-\Delta y}^{\Delta y} \cos\left(\left(\frac{\tilde{l}\pi}{2\Delta y}\right)y - \Delta y\right) p(x, y)dy \tag{3.84}$$

where $p(x, y)$ are the field expressions (eqs (3.72) and (3.74)) derived previously. Substitution of eqs (3.77)-(3.82) into the field expressions and the testing function, the following equations are derived:

$$\alpha_{\tilde{n}} \frac{\tan k_{x1\tilde{n}}\Delta x - \cot k_{x1\tilde{n}}\Delta x}{2k_{x1\tilde{n}}}\, (1 + \delta_{\tilde{n},0})\, \Delta y +$$

$$\beta_{\tilde{n}} \frac{\tan k_{x1\tilde{n}}\Delta x + \cot k_{x1\tilde{n}}\Delta x}{2k_{x1\tilde{n}}}\, (1 + \delta_{\tilde{n},0})\, \Delta y -$$

$$\sum_n \sum_m \alpha_n \frac{\psi^+(m, n)\psi^+(m, \tilde{n}) \cot k_{x2m}\left(\frac{a}{2} - \Delta x\right)}{k_{x2m}\frac{b}{2}\, (1 + \delta_{m,0})} = 0 \tag{3.85}$$

$$\alpha_{\tilde{n}} \frac{\tan k_{x1\tilde{n}}\Delta x + \cot k_{x1\tilde{n}}\Delta x}{2k_{x1\tilde{n}}} (1 + \delta_{\tilde{n},0}) \Delta y +$$

$$\beta_{\tilde{n}} \frac{\tan k_{x1\tilde{n}}\Delta x - \cot k_{x1\tilde{n}}\Delta x}{2k_{x1\tilde{n}}} (1 + \delta_{\tilde{n},0}) \Delta y -$$

$$\sum_n \sum_m \beta_n \frac{\psi^+(m,n)\psi^+(m,\tilde{n}) \cot k_{x2m}\left(\frac{a}{2} - \Delta x\right)}{k_{x2m}\frac{b}{2}(1 + \delta_{m,0})} = 0. \quad (3.86)$$

Finally a matrix equation can be formed from eqs (3.85) and (3.86) and can be written as,

$$A(k_c) \left[\alpha_1 \; ... \; \alpha_n \; \beta_1 \; ... \; \beta_n\right]^T = \mathbf{0} \qquad (3.87)$$

where $A(k_c)$ is a matrix of basis columns and testing rows and $\mathbf{0}$ is specifically the zero vector. The final step is to find the values of k_c that satisfy $\det A = 0$. The method used is to find the eigenvector of $A(k_c)$, which will satisfy the equation. For this thesis, Newton's Method was used by guessing at an initial value and iteration until the determinate that was equal to zero was found. MATLAB was utilized to numerically solve for the cutoff wavenumber or the dominant and next order mode to establish bandwidth.

3.2   Measurement Procedure

The measurement procedures for DRWG and rectangular waveguide are identical in practice. While order is not particularly important, the "thru", "line", and "reflect" measurements described in Section 2.8.1 need to be taken to calibrate the system. Additionally, the sample under test needs to be measured by the system. The physical thicknesses of the line standard and sample also need to be recorded for use in the NRW algorithm described next, although it is possible to determine the line thickness with the thru and line measurements. Upon collection of the data, processing will be accomplished in MATLAB.

One area that has not been addressed is the selection of the line standard. It is desired to have a large sample holder to maximize possible sample thickness, but the width of the holder will be have to be small enough to not cause a phase ambiguity. The first step is to design the length so that it is approximately one quarter of the wavelength at the center

frequency. The next step is to verify that the phase does become ambiguous in the line standard when a wave is propagating through it [9]. Figure 3.2 shows a 7 mm and 9 mm line standard phase plot. As can be seen, the phase for 7 mm does not reach a singularity across the bandwidth as the 9 mm standard does. To maximize sample thickness and to keep a safe margin from the zero phase point, the 7 mm standard was chosen.
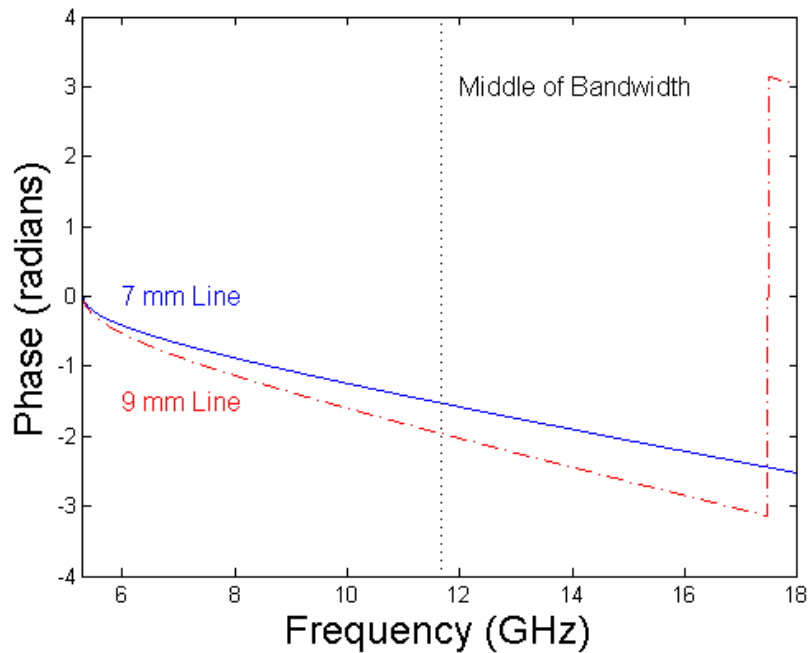

Figure 3.2: Phase Plot Depicting 7 mm and 9 mm Line Standards

3.3   Nicholson-Ross-Weir

The mathematical technique used to derive expressions for the constitutive parameters is called the NRW algorithm. This technique will determine the constitutive parameters from the S-parameters relative to one port at a time. For homogeneous and isotropic media, the parameters should be the same for the opposite port as well. For the following derivation, the S-parameters involved are the forward parameters and represent the calibrated data, denoted as S_{xx}^{exp} [5].

42

The first quantity desired is known as the inter-facial reflection coefficient (R) and is given by

$$R = Q \pm \sqrt{Q^2 - 1}, \tag{3.88}$$

where Q is given by

$$Q = \frac{(S_{11}^{exp})^2 - (S_{21}^{exp})^2 + 1}{2S_{11}^{exp}}. \tag{3.89}$$

Equation 3.89 has two solutions that are related as inverses. One solution will have a magnitude less than one and is the solution used to proceed. The next step is to determine the one-way phase delay, denoted as P, and is given by

$$P = \frac{S_{21}^{exp}}{1 - RS_{11}^{exp}}. \tag{3.90}$$

The cutoff frequency for rectangular waveguide was given in the previous chapter (2.24). Applying (2.24) to a TE_{10} mode wave, the cut off frequency, k_0 and γ_0 are given by

$$k_c^2 = \frac{\pi^2}{a^2} , \; k_0^2 = \omega^2 \epsilon_0 \mu_0 , \; \gamma_0^2 = k_c^2 - k_0^2 \tag{3.91}$$

where a is the long dimension of the waveguide and ω is the angular frequency ($\omega = 2\pi f$). The final step in the NRW algorithm to find the constitutive parameters. The relative permittivity (ϵ_r) is given by

$$\epsilon_r = -\frac{k_c^2 - ((\ln P)/l)^2}{k_0^2 \frac{\ln P}{\gamma_0 l}\left(\frac{1+R}{1-R}\right)} \tag{3.92}$$

where l is the thickness of the sample [10]. The relative permeability (μ_r) is then computed as

$$\mu_r = \frac{c \ln P}{\gamma_0 l}\left(\frac{1+R}{1-R}\right). \tag{3.93}$$

The constitutive parameters can be determined separately for forward (S_{11}, S_{21}) or reverse parameters (S_{22}, S_{12}), by simply substituting the correct reflection/transmission parameters above (S_{22} for S_{11} and S_{12} for S_{21}). Since the calibration planes are set at either side of the sample holder, it is also necessary to calculate the phase delay from either port to the
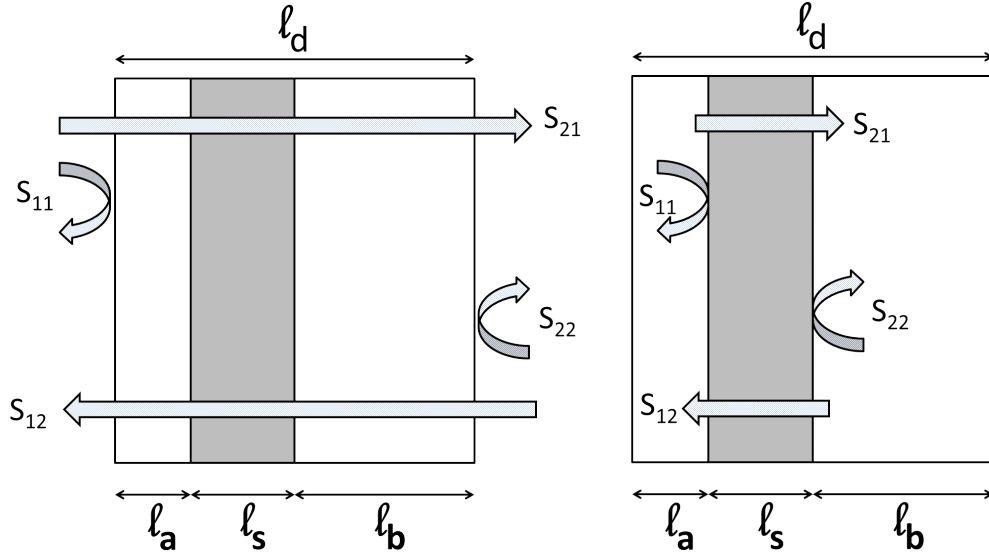
(a) S-parameters calibrated to cal planes   (b) S-paremters shifted to sample

Figure 3.3: S-Parameter Calibration and Adjustment

sample and back. To calculate the phase delay, the path to and from the sample will be accounted for. In Figure 3.3(a), the calibration planes are the edges of the holder. The scattering parameters measured are shown and an adjustment must be made to account for displacement of the sample. Starting with S_{11} and S_{21},

$$S_{11} = e^{-jk_{z0}\ell_a} S_{11}^{sample} e^{-jk_{z0}\ell_a} \tag{3.94}$$

$$S_{21} = e^{-jk_{z0}\ell_a} S_{21}^{sample} e^{-jk_{z0}\ell_b}, \tag{3.95}$$

where k_{z0} is the propagation wavenumber in free space and the other variables correspond to the values in Figure 3.3. The goal is to obtain the S-parameters for the sample, so solving for S_{11}^{sample} and S_{21}^{sample},

$$S_{11}^{sample} = S_{11} e^{j2k_{z0}\ell_a} \tag{3.96}$$

$$S_{21}^{sample} = S_{21} e^{jk_{z0}(\ell_h - \ell_s)} \tag{3.97}$$

44

and the forward parameters are found. Following a similar process for the reverse parameters will show,

$$S_{22}^{sample} = S_{22}e^{j2k_{z0}\ell_b} \tag{3.98}$$

$$S_{12}^{sample} = S_{12}e^{jk_{z0}(\ell_h-\ell_s)}. \tag{3.99}$$

The phase adjustment for the S-parameters has been adjusted to the sample itself instead of the sample holder and the constitutive parameters can be extracted using the NRW algorithm.

3.4   Sample Preparation

For this work, there were two materials measured. The first was a plastic material provided by Air Force Research Laboratory (AFRL), an acrylic sample and two different microwave absorbers. The sample constructed by AFRL is a polymer known commercially as VeroP and was fabricated in a Polyjet 3D printer. The design was accomplished in Solidworks and is shown in Figure 3.4. The dimensions used to draw the sample were taken from datasheets for WRD-650. The dimensions of the final product were slightly bigger than the guide. Since tight samples are desired for maximum accuracy, the samples were forced into the line standard. This was only attempted because the size of the sample was extremely close to the size of the guide. The result was that some of the excess material was shaved off of the sample by the line standard and the sample fit extremely tight in the waveguide. This process was repeated for each sample with similar results. In order to verify the designs prior to sending out for fabrication by AFRL, an acrylic sample was made using local 3D printer resources. The acrylic was able to fit similarly to the AFRL sample.

The absorber material was formed using laser cut plastic as a template, then cut out using a razor. The same procedure of pushing the line standard onto the sample was performed. The original thought process was similar to that of the more rigid plastic

45
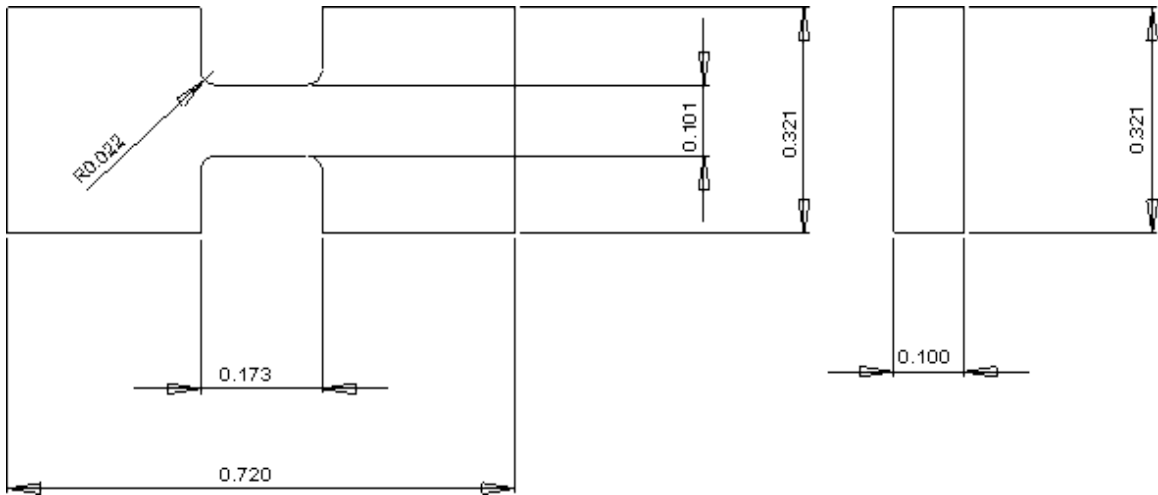
Figure 3.4: Sample Drawing (Values in Inches)

samples; the material would nicely shave off and fit well into the guide. This was not true in practice, especially with the thicker absorber material tested. The results of each method will be discussed and testing in depth in the next chapter.

IV.   Results

THIS chapter will focus on the extraction of the constitutive parameters from material samples.   All of the measurements were performed using the Agilent E8362B NWA.   The measurements were taken in the frequency domain from 6-18GHz.   For each measurement, the four scattering parameters were measured, in addition to the port mis-match power ratios at each detector.   External calibration was conducted using a "Thru", "Line" and "Reflect" measurement.   The cutoff frequency is also determined using MATLAB code and the bandwidth of DRWG is demonstrated.   Uncertainty in the measurements will be presented in the propagation of error method.   Comparisons to rectangular waveguide measurements will be demonstrated and challenges that presented in the experimentation will be discussed.

4.1   Bandwidth

From Section 2.6, a table of usable bandwidth existed for DRWG and rectangular waveguide. Table 4.1 shows the bandwidth calculated using the MATLAB code to find the cutoff frequency.

Table 4.1: Calculated DRWG Bandwidth

WRD-650		
Dominate Mode Cutoff	Next Order Cutoff	Bandwidth
5.303 GHz	18.291 GHz	12.988 GHz

Mathematically, there should be approximately 13 GHz of bandwidth available for use from DRWG. In reality, a safety factor needs to be established from the cutoff frequency for usable bandwidth. Figure 4.1 shows a vertical line at the calculated cutoff of 5.303 GHz. The manufacturers suggested lower band is also shown at 6.5 GHz. While 6.5 GHz
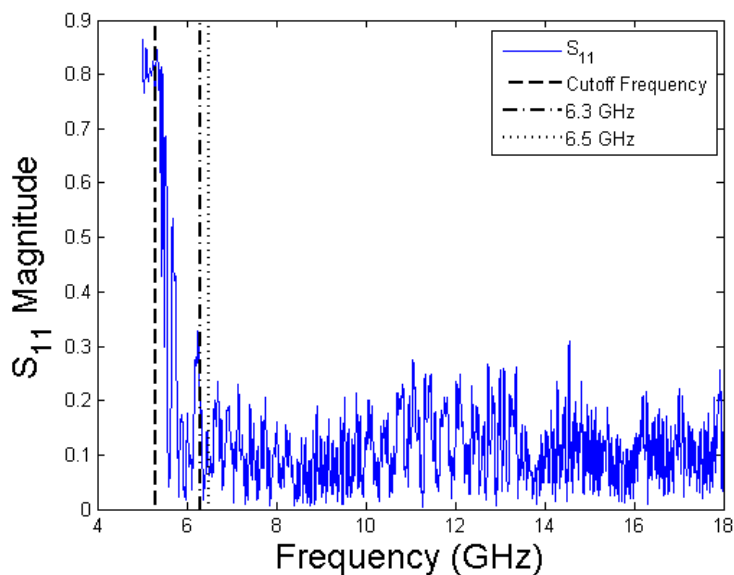
Figure 4.1: Cutoff Frequency Illustration Using Uncalibrated Data

is free from errors exhibited by the lower cutoff, 6.3 GHz is an approximate 1.2x safety factor. Therefore, the measurement bandwidth presented will range from 6.3 GHz to 18 GHz.

4.2 Uncertainty in Measurements

While waveguides can provide good measurements, uncertainty will manifest in multiple places. The technique used to quantify uncertainty will be a propagation of error technique, since a statistically significant number of measurements is not practical in the measurement technique used here [7]. The types of uncertainty that will arise from the system, the sample, the sample position, the holder and the waveguide tolerances are discussed. This section will also display results with uncertainty factored in as error bars. All of the uncertainty values used are displayed in Table 4.2. Additionally, all of the values shown represent a worst-case scenario for uncertainty.

Table 4.2: Uncertainty Values

Uncertainty Type	AFRL Sample	Acrylic	SF-3.0	FGM-125
$|S_{11}|$	0.01125	0.01125	0.02	0.02
$\angle S_{11}$	1.6°	1.6°	1.6°	1.6°
$|S_{21}|$	0.1dB	0.1dB	0.06dB	0.06dB
$\angle S_{21}$	0.3°	0.3°	0.5°	0.8°
Position	0.01 mm	0.01 mm	0.05 mm	0.10 mm
Thickness	0.01 mm	0.01 mm	0.05 mm	0.05 mm
Holder Width	0.035 mm	0.035 mm	0.035 mm	0.035 mm
k_c	5%	5%	5%	5%

4.2.1 *System Uncertainty.*

The NWA has separate published uncertainties for reflection and transmission coefficients. For the NRW algorithm, there is interest in the phase and magnitude uncertainty for both coefficients. The values of the uncertainty can be extracted from the users manual provided on the NWA as plots [1]. The worst case values were used for the results in this work. In Table 4.2, the system uncertainty is the first four rows where $|S_{11}|$ and $\angle S_{11}$ are the reflection uncertainties in magnitude and phase respectively. $|S_{21}|$ and $\angle S_{21}$ denote the transmission uncertainties in magnitude and phase.

4.2.2 *Sample and Sample Holder Uncertainty.*

The sample under test needs to be measured and those values are used in the NRW algorithm. Sample thickness and dimensions will have some sort of uncertainty associated with them. For this analysis, only the sample thickness will be taken into consideration since the waveguide will determine the other dimensions. The sample thickness varied for the type of material. The rigid materials (AFRL sample and acrylic) did not vary in thickness and their overall uncertainty was set at the lowest possible resolution of the

Figure 4.2: A Single Sample with Two Thicknesses

calipers used to make the measurement. The microwave absorber materials were not as straightforward to measure. In some cases, a single sample presented a gradient across the dimensions as seen in Figure 4.2.

In addition to the sample itself, there is also some uncertainty in the placement of the sample in the waveguide. When installing the sample into the holder, efforts are made to make sure the face of the sample is flush with the face of the guide. The sample holder is placed on a flat surface and the sample under test is forced down so the displacement from one side is very close to zero. Again, there was a difference in uncertainty for the ridged materials and the softer materials. The rigid materials presented a measured uncertainty of less than the machine precision of the calipers, while the softer materials varied in position slightly more.

The sample holder itself also has some uncertainty associated with it. To find an uncertainty term, the line and thru measurements were used. The line length can be calculated by using the phase delay found by comparing the two measurements. Recall,

$$\widetilde{\mathbf{T}}^{A^{-1}}\mathbf{M}\widetilde{\mathbf{T}}^{A} = \mathbf{T}^{\ell} = \begin{bmatrix} e^{-jk_z\ell} & 0 \\ 0 & e^{jk_z\ell} \end{bmatrix} \tag{4.1}$$

50

from Section 2.8.1.2. By finding the eigenvector of the left side, an overdetermined solution will result and ℓ, the line length, can be solved for. This results in an electric measurement over the bandwidth of interest, which is shown in Figure 4.3. Taking the standard deviation of the data plotted is the uncertainty value used here.
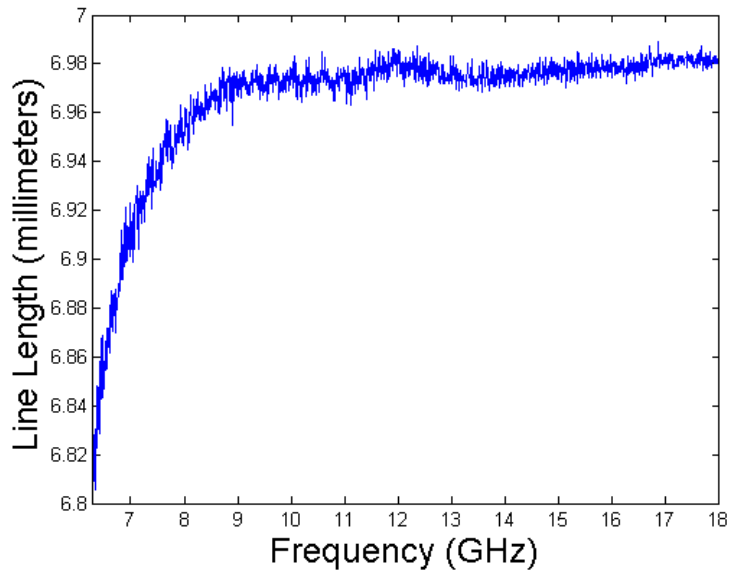
Figure 4.3: Line Length Calculated Using Thru and Line Measurements

4.2.3 Waveguide Tolerance Uncertainty.

The waveguide itself has an uncertainty due to imperfect manufacturing. The primary effect of imperfect dimensions on uncertainty is in the cutoff wavenumber, k_c. While the ideal DRWG will have completely square corners on the ridges, the actual physical specimens are not square due to limitations in machining tools and fabrication techniques. The perfect specimen is shown in Figure 4.4(a) and the actual product is shown in Figure 4.4(b). The implications of the imperfect waveguide will impact the actual value of k_c, as well as make sample fabrication more challenging. The value by which k_c will differ is approximately 5%, as determined by another technique of determination [12]. The
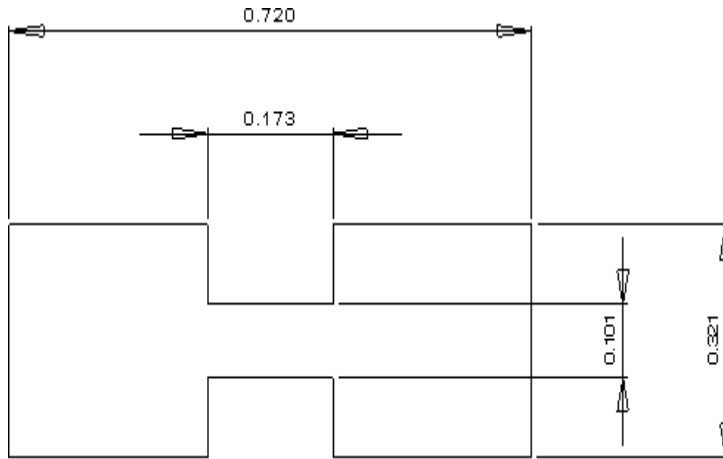
(a) Square Corners
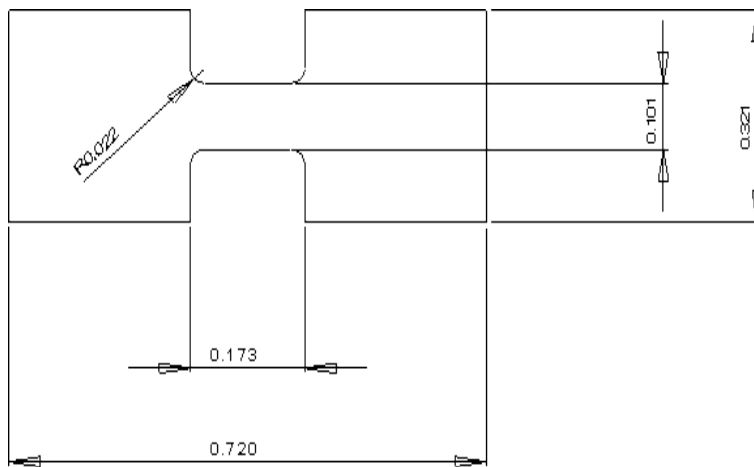
(b) Rounded Corners

Figure 4.4: DRWG Configurations for Analysis

rounded corners will actually drive the cutoff frequency up, which will also have the effect of decreasing the bandwidth slightly.

4.2.4 Application of Uncertainty Terms.

The uncertainty method used here will act on the constitutive parameter equations. Each uncertainty term will be calculated and added in quadrature. The formula used to

calculate the propagation of uncertainty will be,

$$\sigma_{\epsilon_r^r}^2 = \overbrace{\underbrace{\left(\frac{\partial \epsilon_r^r}{\partial |S_{11}|}\sigma_{|S_{11}|}\right)^2}_{Magnitude\ Term} + \underbrace{\left(\frac{\partial \epsilon_r^r}{\partial \angle S_{11}}\sigma_{\angle S_{11}}\right)^2}_{Phase\ Term}}^{Reflection\ Terms} + \overbrace{\underbrace{\left(\frac{\partial \epsilon_r^r}{\partial |S_{21}|}\sigma_{|S_{21}|}\right)^2}_{Magnitude\ Term} + \underbrace{\left(\frac{\partial \epsilon_r^r}{\partial \angle S_{21}}\sigma_{\angle S_{21}}\right)^2}_{Phase\ Term}}^{Transmission\ Terms} +$$

$$\underbrace{\left(\frac{\partial \epsilon_r^r}{\partial \ell}\sigma_\ell\right)^2}_{Sample\ Length} + \underbrace{\left(\frac{\partial \epsilon_r^r}{\partial d}\sigma_d\right)^2}_{Line\ Length} + \underbrace{\left(\frac{\partial \epsilon_r^r}{\partial k_c}\sigma_{k_c}\right)^2}_{Cutoff} + \underbrace{\left(\frac{\partial \epsilon_r^r}{\partial \ell_{holder}}\sigma_{\ell_{holder}}\right)^2}_{Position\ Term} \quad (4.2)$$

where S_{11} and S_{21} have magnitude and phase components and ℓ, d and k_c are the sample length, line length and cutoff wavenumber uncertainties respectfully. Similar equations are also applied for the imaginary part of the permittivity (ϵ_r^i) and both parts of the permeability (μ_r^r and μ_r^i).

4.3   Measured Sample Results

For the AFRL sample, the measurements with uncertainty are shown in Figures 4.5(a) and 4.5(b). As can be seen in Figure 4.5(b), the relative permeability uncertainty (μ_r) is fairly sensitive to changes in k_c at the lower frequencies. The results show a uniform response across the bandwidth. The overall uncertainty is low across the bands due to small sample uncertainties as discussed about the rigid samples.

During the sample fabrication process, the 3D printer from Air Force Institute of Technology (AFIT) was used to verify the sample size. The material used is a commercially available acrylic. The constitutive parameters for this material are shown in Figures 4.6(a) and 4.6(b). The results show that the material has a fairly uniform response across the bandwidth that closely resembled the sample from AFRL. Again, the overall uncertainty is low for low sample uncertainties.

Both of the rigid samples above have very similar electrical properties. They are both polymers that were made on similar 3D printer machines. As stated, fabrication was made for this work specifically. Not all measurement situations will allow a sample to be easily
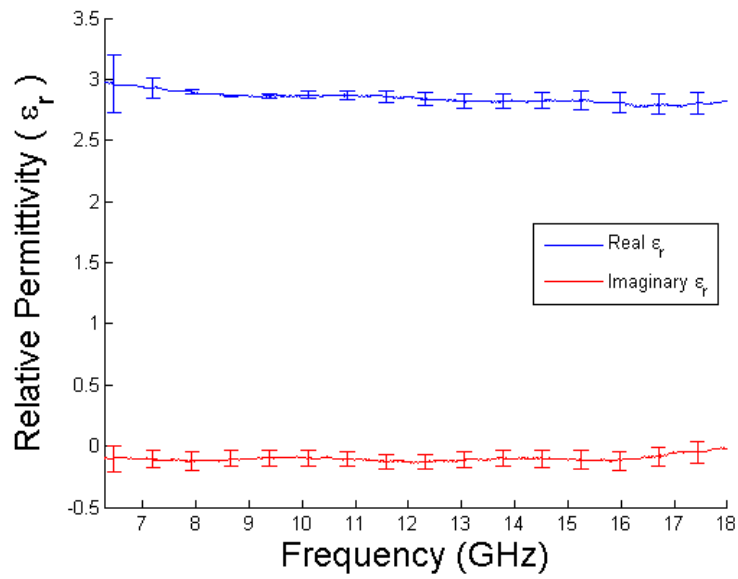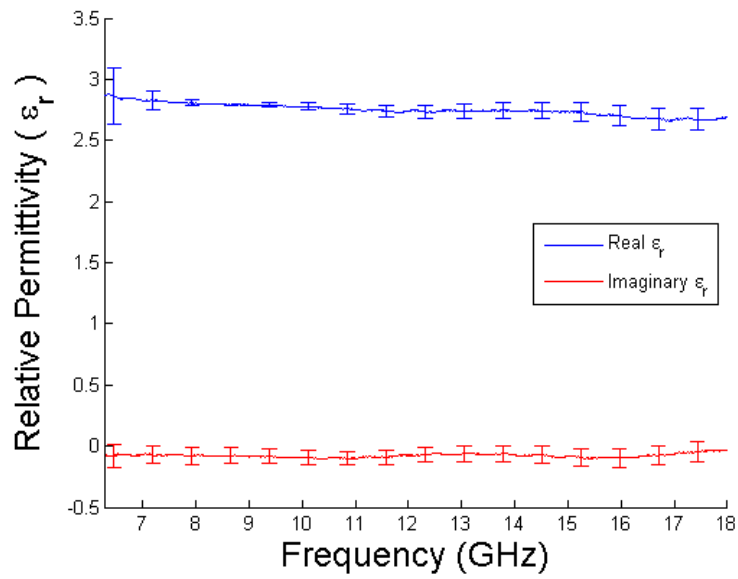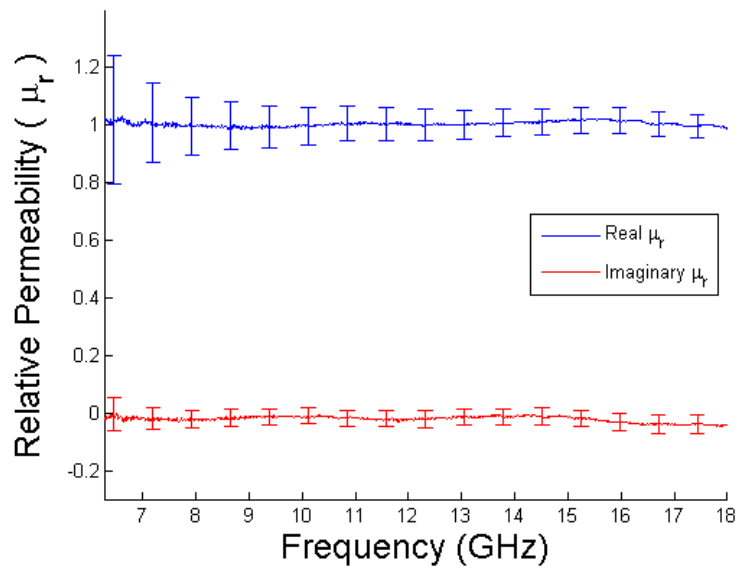
(a) AFRL Sample Results with Uncertainty (ϵ_r)
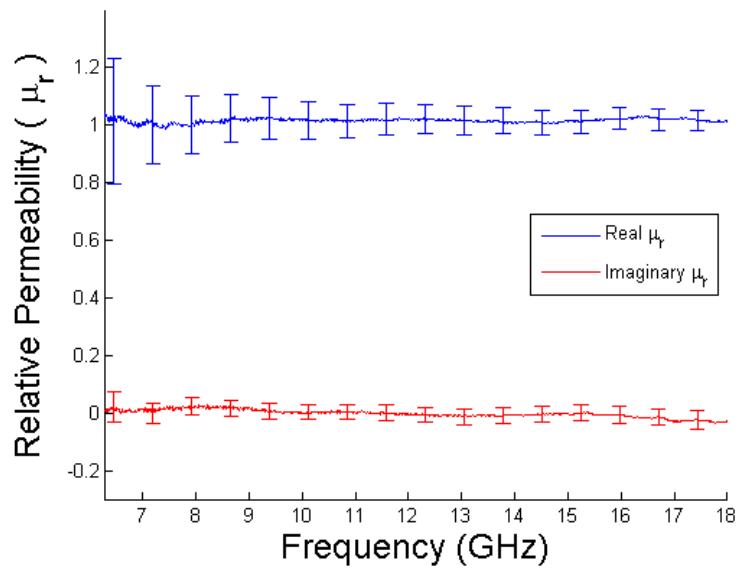
(b) AFRL Sample Results with Uncertainty (μ_r)

Figure 4.5: AFRL Sample Results

fabricated by precision machinery, so attempting to measure non-rigid, custom cut pieces seems to be a more realistic application.
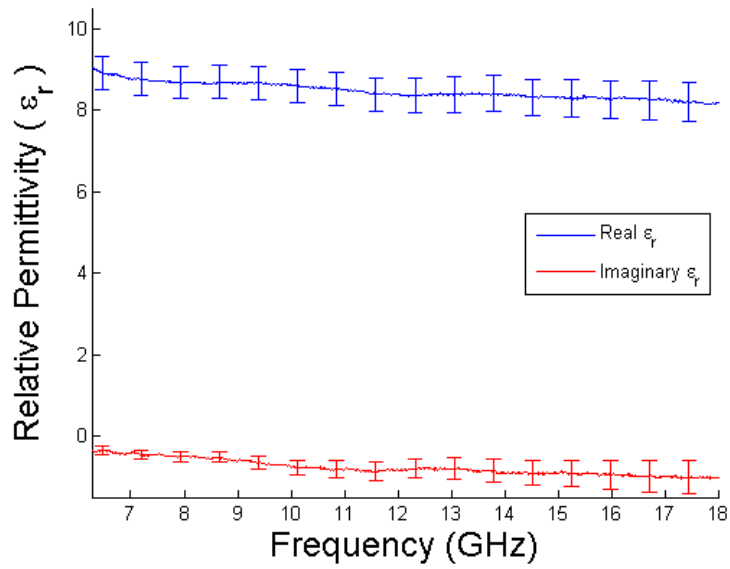
(a) Acrylic Sample Results with Uncertainty (ϵ_r)
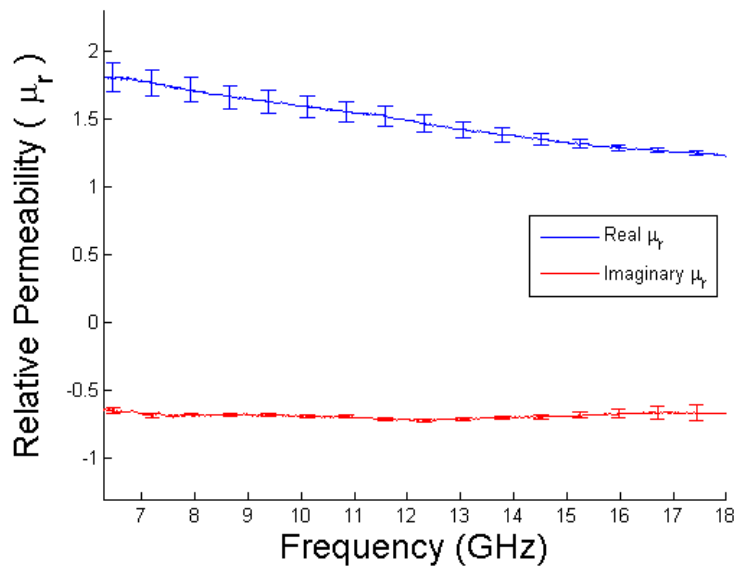

(b) Acrylic Sample Results with Uncertainty (μ_r)

Figure 4.6: Acrylic Results

Upon initial observations, the microwave absorber was simple to cut and shape into a quality measurement specimen. While measuring, it was quickly discovered that the

(a) SF-3.0 Absorber Results with Uncertainty (ϵ_r)

(b) SF-3.0 Absorber Results with Uncertainty (μ_r)

Figure 4.7: SF-3.0 Results

fabrication process benefits drastically by having a close attention to detail. The easiest of the two materials used was the SF-3.0 from ECCOSORB. It is thin and easy to cut, making
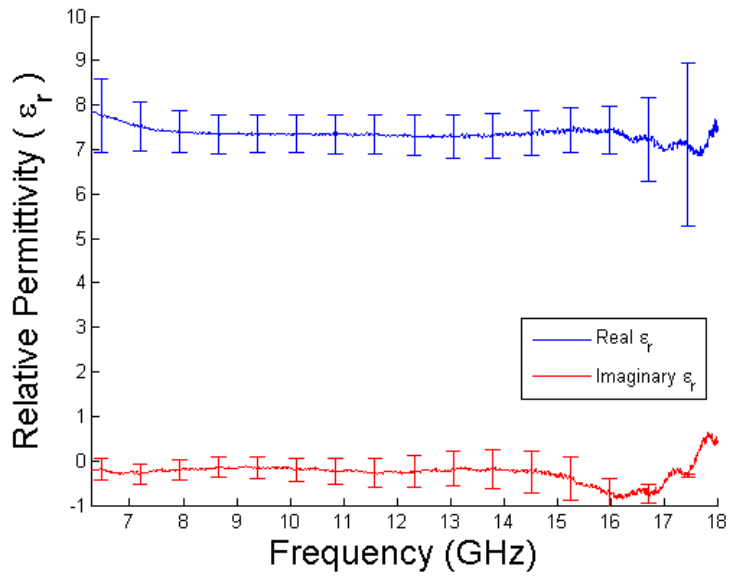
(a) FGM-125 Absorber Results with Uncertainty (ϵ_r)
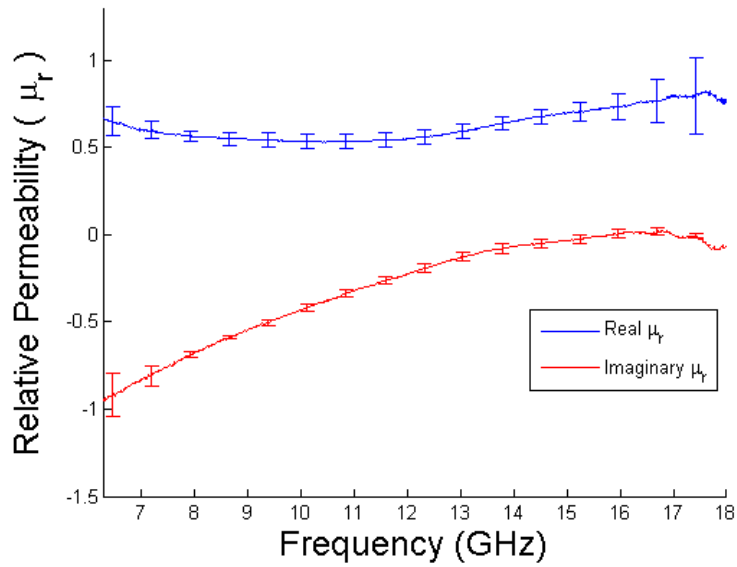
(b) FGM-125 Absorber Results with Uncertainty (μ_r)

Figure 4.8: FGM-125 Results

it straightforward to fabricate. The results of measurement are displayed in Figures 4.7(a) and 4.7(b). The final material measured was ECCOSORB FGM-125, a commercially

available microwave absorber. The results from the FGM-125 are shown in Figures 4.8(a) and 4.8(b). The variance and difficulties of shaping this material by hand are discussed in the next section.

4.4   Sample Modification

Great difficulty was encountered in fabricating flexible material samples. The FGM-125 proved to be the most difficult. The measurements would show problems in the higher frequency range, particularly around 16 GHz and up. Initially, this issue was falsely assumed to a problem discussed in Section 4.6 that was discovered previously. Upon observation of some poorly made sample post technique improvement, it was discovered that the sample is very sensitive to flaws. Figure 4.9 shows a small gap on one side of the ridge and Figures 4.10 and 4.11 show the results of the flaw in the measurement.
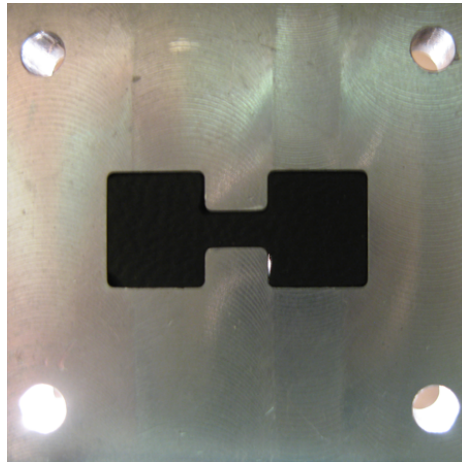
Figure 4.9: Poorly Made Sample

To further understand the sensitivity to sample fabrications, some more specimens were modified in exaggerated ways to observe the behavior. The first modification was to cause a large hole around the ridge. An otherwise well fabricated sample was cut out and then modified as shown in Figure 4.12 and the measurements are shown in Figures 4.13 and 4.14.
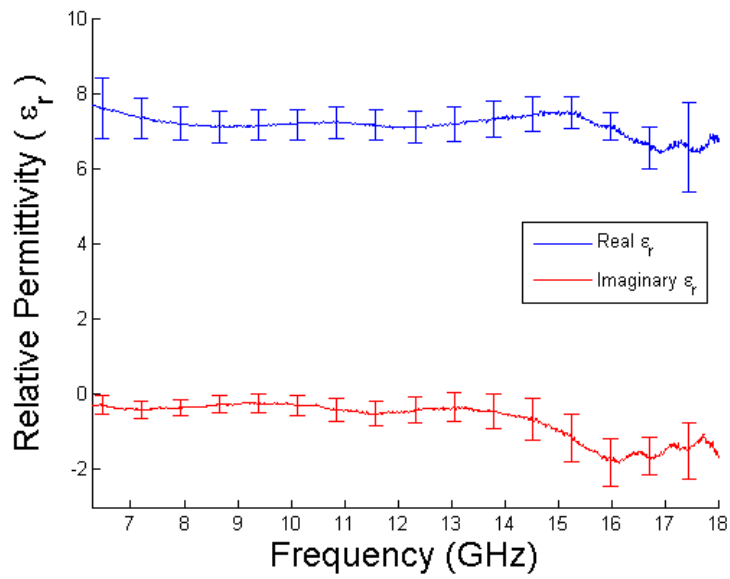
Figure 4.10: Poorly Fabricated Sample: Relative Permittivity
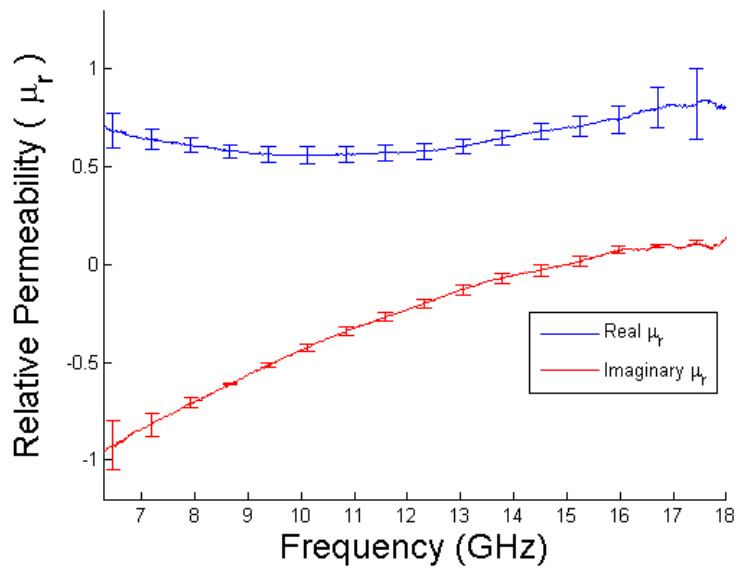
Figure 4.11: Poorly Fabricated Sample: Relative Permeability

Finally, modifying the troughs (or ears) of the guide were investigated (Figures 4.15, 4.16 and 4.17). Judging by the results, the overall permittivity was driven down while the
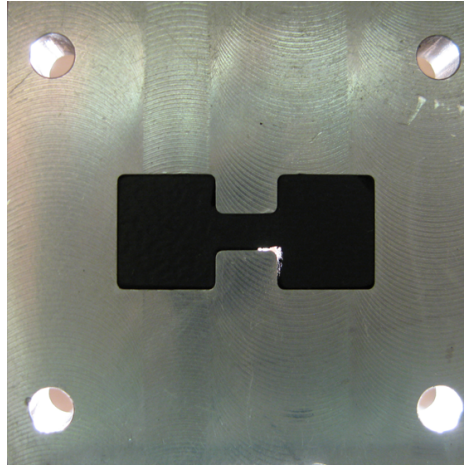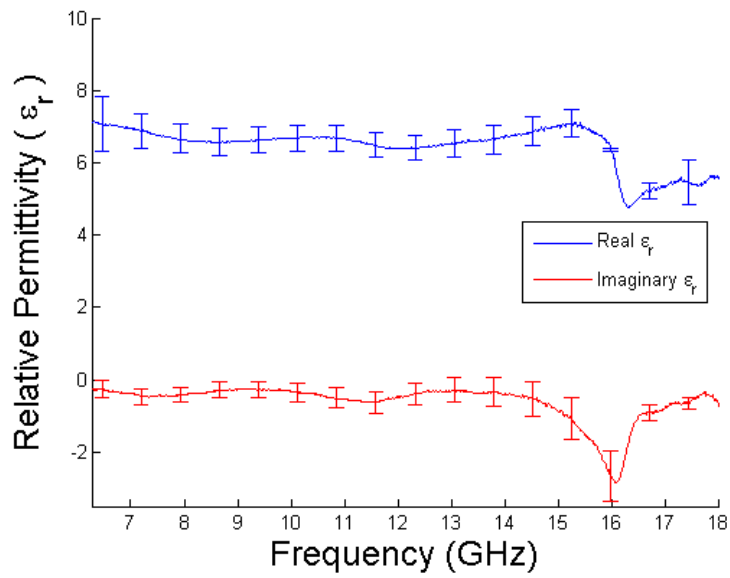
Figure 4.12: Modified Ridge Sample

Figure 4.13: Modified Ridge Sample: Relative Permittivity

results in general were completely unreliable for the higher frequencies. This error and the associated uncertainty could be a limiting factor for making reliable measurements with DRWG particularly at higher portion of the bandwidth.
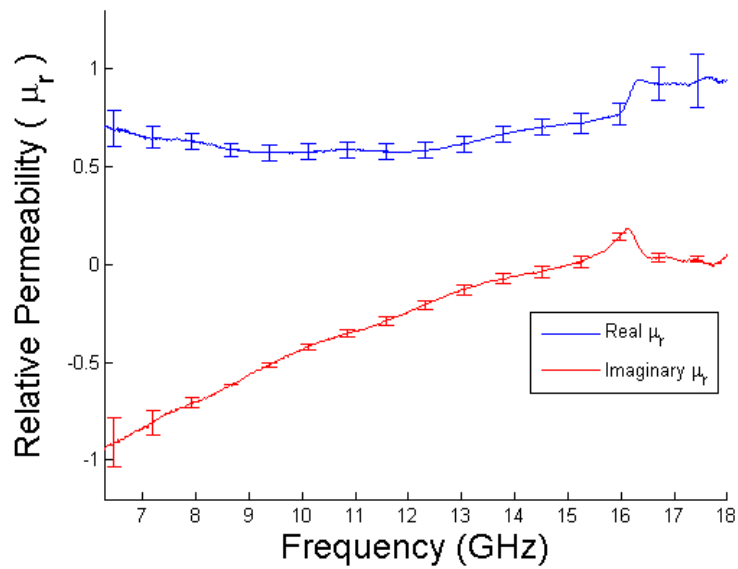
Figure 4.14: Modified Ridge Sample: Relative Permeability
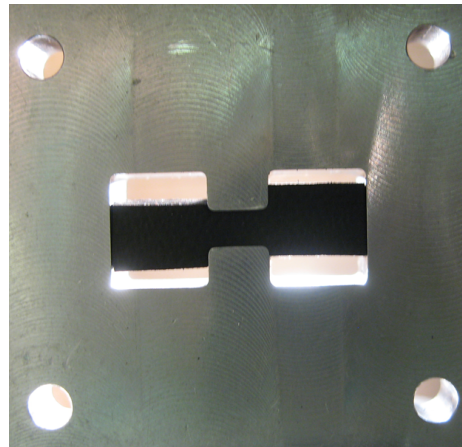
Figure 4.15: Modified Trough Sample

In addition to the problems discussed above, there were also challenges met with the sample fitting too tightly in the guide. This caused compression in the sample, which will negatively affect the measurement. In addition to the compression causing changes in the
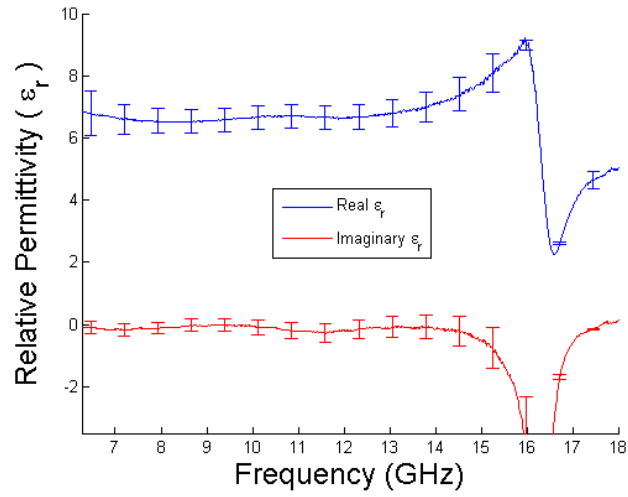
61

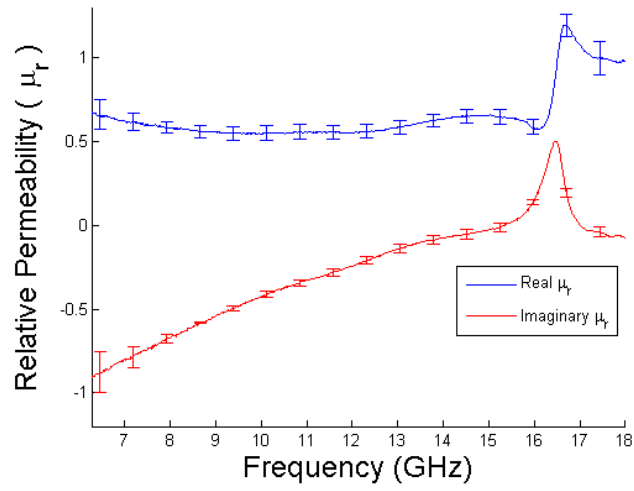Figure 4.16: Modified Trough Sample: Relative Permittivity

Figure 4.17: Modified Trough Sample: Relative Permeability

constitutive parameters, it was also applied non-uniformly across the sample. The results were essentially useless since no accurate sample thickness could be applied.

4.5 Comparison to Rectangular Waveguide

To validate the methodology presented here, the AFRL sample was also measured with rectangular waveguide. While the samples were not the same thickness or made at the same time, the results should show similarities. These results are shown in Figures 4.18 and 4.19. The overall comparison is well within any uncertainty. The rectangular waveguide seems to validate using DRWG as a measurement apparatus.
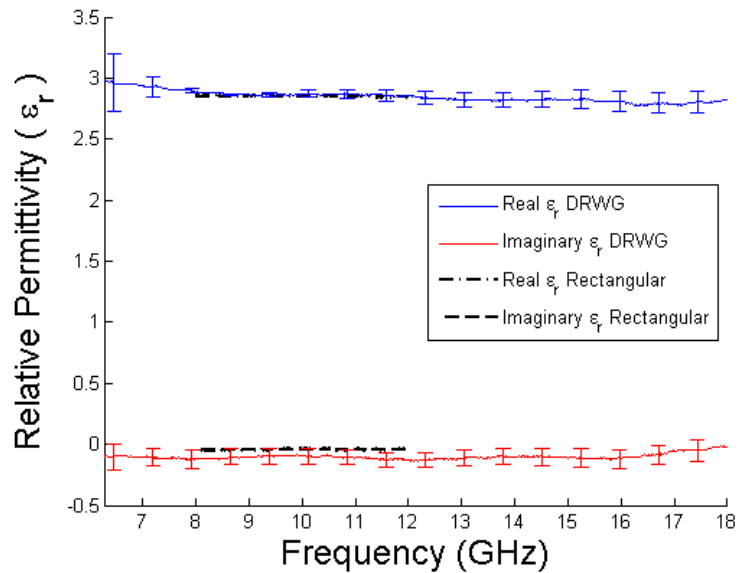

Figure 4.18: DRWG Compared with Rectangular Waveguide Measurement (ϵ_r)

4.6 Additional Challenges in Measurement

Unique challenges exist in DRWG measurements with regard to the higher measurement frequencies, in comparison to rectangular waveguide. Initial results were plagued by a common decrease in the final measurement at approximately 16 GHz (Figure 4.20), which is a higher band than is measurable by X-band waveguide. After some extended experimentation, it was discovered that the uncalibrated data displayed the same decrease (Figure 4.20), indicating a problem in the measurement technique or a piece of equipment. Two problems were identified: inconsistent clamping pressure and a damaged reflect standard.
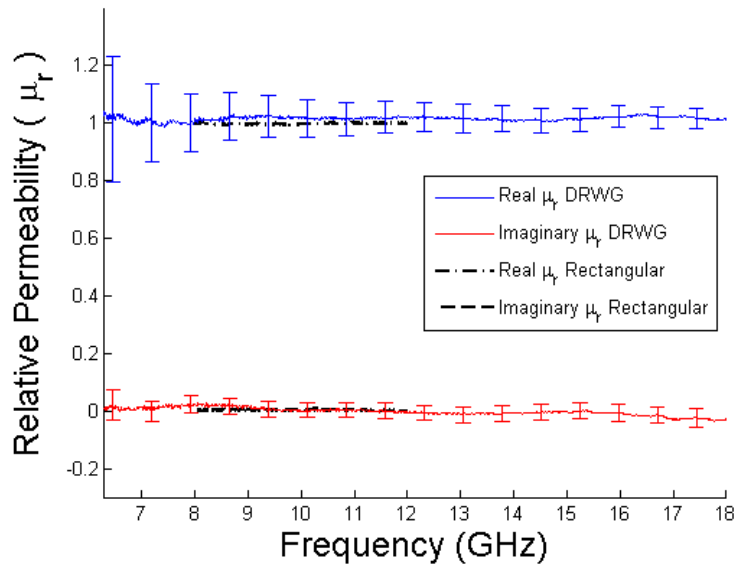
63

Figure 4.19: DRWG Compared with Rectangular Waveguide Measurement (μ_r)

Upon close inspection, one of the reflect standards had a slight curve in it (Figure 4.21). This was causing a slight cavity response and defeating the assumption of a zero offset short in the TRL calibration. The small curve was shown by placing a razor blade across the standard and observing light coming though. The non-curved reflect standard shows a little light coming through, where the razor has some slight imperfections. The curved reflect standard shows a significant amount of light passing under the blade, thus illustrating a significant problem.

While the solutions described above seemed to mitigate measurement problems in the rigid samples, they did not solve the all of the problems with the absorbers. Close inspection of the samples revealed a two major problems. The first was simply poor fabrication that resulted in some unwanted gaps between the material and sample holder. The second problem was identified by measuring the sample thickness while in the holder. The thickness was actually slightly larger than when outside of the guide, indicating compression of the sample. The dimensions of the sample were reduced by carefully
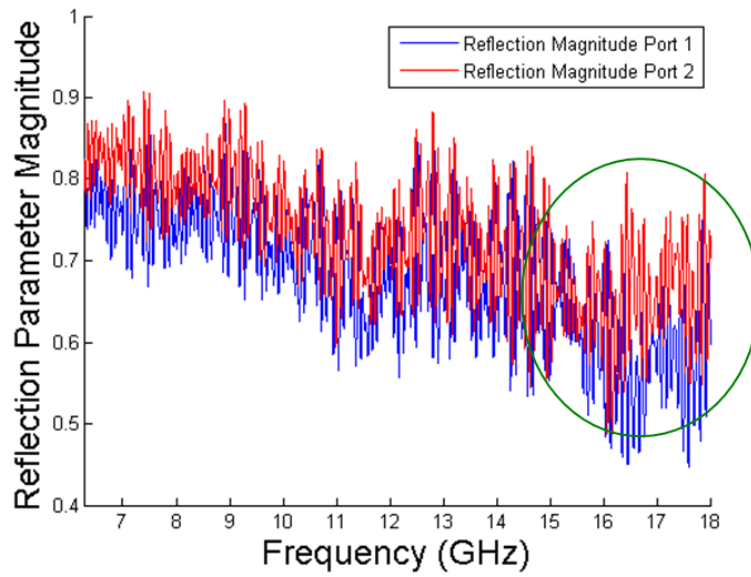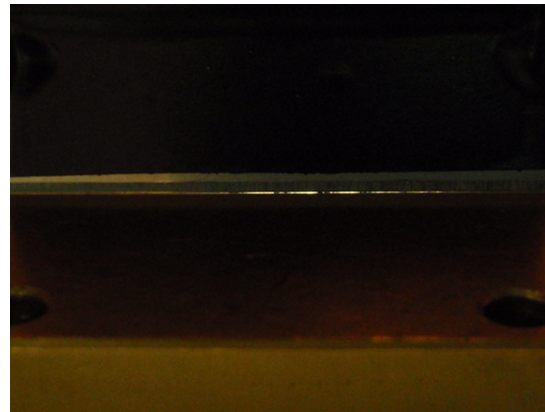
64

Figure 4.20: Curved Reflect Standard vs. Flat Standard Raw Data

(a) Curved Reflect Standard   (b) Flat Reflect Standard

Figure 4.21: Reflect Standard Comparison

scraping material off with a razor knife until the thickness of the sample did not change when it was inserted into the holder. Care was also taken to take minimal material off of the ridged portions, while still slightly reducing the overall size.

V. Conclusion

THE method of using DRWG was presented for gathering constitutive parameter data about a material. The method required some knowledge about other methods, particularly rectangular waveguide measurements, to appreciate the advantages of using DRWG. While a significant advantage of using DRWG is an increased bandwidth measurement range, the disadvantages were not trivial. Material samples in particular were much more difficult to fabricate. The samples measured included a AFRL provided dielectric and an acrylic sample that both demonstrated fairly constant constitutive parameters across the measurement band. The other samples measured included two commercially available microwave absorbers that demonstrated dynamic parameters across the bandwidth.

In order to understand the purpose of the measurements, a brief electromagnetics overview was presented. To appreciate the gathering of data, a calibration technique known as TRL was discussed and derived using different measurement configurations. Because the cutoff frequency was important for the NRW algorithm to calculate the constitutive parameters, a detailed analysis of DRWG was performed. Results were presented to include uncertainties in the measurements and comparison to rectangular waveguide.

5.0.1 Sample Fabrication.

Sample preparation was one of the most challenging aspects of the work performed here. For rectangular waveguide, samples can be easily fabricated from larger specimens of the sample material with straight razor blade. While AFRL is able to easily grow a sample to exact specifications and dimensions, this may not be practical in some laboratory environments or possible with most materials. With a soft material such as the microwave absorber presented here, a rough template can be cut with a sharp blade and then forced into a line standard. A harder material, such as the AFRL sample, can be formed in a

66

similar fashion, but the template must be more exact. Some tooling could possibly be used, such as an end mill, but the final cut would have to be forced into the line standard. If this method is to be used, it may be prudent to have a line standard made out of a harder metal that could prove to be more robust when cutting samples. Additionally, perhaps some sort of die could be made to cut the samples.

5.0.2   *Non Destructive Testing.*

One of the major deficiencies in the type of measurement presented here is the fact that the original test article is destroyed in the process of taking a measurement. Harvesting samples from the LO treatment on an aircraft is not usually done in practice, since extensive and expensive repair work would be required. In addition to the need to harvest some material, the samples may not hold up to repeated measurements taking place. Because of the low tolerances allowed around the sample in the holder, a few of the AFRL samples were broken due to repeated extractions from the line standard. A non destructive method to measure samples could be more convenient and would make taking measurements much more simple and has been demonstrated using rectangular waveguide.

Bibliography

[1] Agilent Technologies. *Agilent PNA Series Network Analyzer Manual*, September 2012.

[2] Baker-Jarvis, James. *Transmission/Reflection and Short-Circuit Line Methods for Measuring Permittivity and Permeability*. Technical report, United States Department of Commerce, 1993.

[3] Balanis, Constantine A. *Advanced Engineering Electromagnetics*. Wiley and Sons, Inc., 1989.

[4] Balanis, Constantine A. *Antenna Theory*. John Wiley and Sons, Inc, 3rd edition, 2005.

[5] Chen, L.F. *Microwave Electronics: Measurement and Materials Characterization*. Wiley, 2004.

[6] Cobham Defense Electronic Systems. *Waveguide Component Specifications and Design Handbook*, 7 edition.

[7] Coleman, Hugh W. *Experimentation, Validation, and Uncertainty Analysis for Engineers*. Wiley, 2009.

[8] Collin, Robert E. *Field Theory of Guided Waves*. The Institute of Electrical and Electronics Engineers, 1991.

[9] Engen, Glenn F. and Cletus A. Hoer. "Thru-Reflect-Line: An Improved Technique for Calibrating the Dual Six-Port Automatic Network Analyzer". *IEEE Transactions Microwave Theory and Techniques*, 1979.

[10] Gunn, William E. *Application of the Three Short Calibration Technique in a Low Frequency Focus Beam System*. MS thesis, AFIT/GE/ENG/10-10. Air Force Institute of Technology (AU), Wright-Patterson AFB OH, March 2010.

[11] Harrington, Roger F. *Time-Harmonic Electronic Fields*. McGraw-Hill Book Company, 1961.

[12] Hyde, Milo W. "Broadband Characterization of Materials Using Dual-Ridged Waveguide". *IEEE Transactions on Instruments and Measurement*, 2013.

[13] Jeffrey, Alan. *Advanced Engineering Mathematics*. Academic Press, 2001.

[14] Microwave Engineering Corporation. *Double Ridged Waveguide Datasheet, T22D*.

[15] Montgomery, James P. "On the Complete Eigenvalue Solution of Ridged Waveguide". *IEEE Transactions on Microwave Theory and Techniques*, MTT-19(6), June 1971.

[16] Musil, J. and F. Zacek. *Microwave Measurements of Complex Permittivity by Free Space Methods and Their Applications*. Elsevier, 1986.

[17] Nicholson, A.M. and G.F. Ross. "Measurement of the Intrinsic Properties of Materials by Time-Domain Techniques". *IEEE Transaction on Instrumentation and Measurement*, 1970.

[18] Pozar, David M. *Microwave Engineering*. John Wiley and Sons, Inc., 2005.

[19] Rytting, Douglas. "Network Analyzer Error Models and Calibration Methods". White Paper from Agilent Technologies, September 1998.

[20] Sun, Weimin and Constantine A. Balanis. "MFIE Analysis and Design of Ridged Waveguides". *IEEE Transactions on Microwave Theory and Techniques*, 41, 1993.

[21] Weir, W. B. "Automatic Measurement of Complex Dielectric Constant and Permeability at Microwave Frequecies". *Proceedings of the IEEE*, 1974.

REPORT DOCUMENTATION PAGE

Form Approved
OMB No. 0704–0188

1. REPORT DATE *(DD–MM–YYYY)*	2. REPORT TYPE	3. DATES COVERED *(From — To)*
21–03–2013	Master's Thesis	Oct 2011–Mar 2013

4. TITLE AND SUBTITLE

Constitutive Parameter Measurement Using Double Ridge Waveguide

5a. CONTRACT NUMBER

5b. GRANT NUMBER

5c. PROGRAM ELEMENT NUMBER

6. AUTHOR(S)

Lehman, Nathan J., Captain, USAF

5d. PROJECT NUMBER

5e. TASK NUMBER

5f. WORK UNIT NUMBER

7. PERFORMING ORGANIZATION NAME(S) AND ADDRESS(ES)

Air Force Institute of Technology
Graduate School of Engineering and Management (AFIT/EN)
2950 Hobson Way
WPAFB, OH 45433-7765

8. PERFORMING ORGANIZATION REPORT NUMBER

AFIT-ENG-13-M-30

9. SPONSORING / MONITORING AGENCY NAME(S) AND ADDRESS(ES)

Air Force Research Laboratory
Sensors Directorate
2591 K Street
WPAFB, OH 45433

10. SPONSOR/MONITOR'S ACRONYM(S)

11. SPONSOR/MONITOR'S REPORT NUMBER(S)

12. DISTRIBUTION / AVAILABILITY STATEMENT

DISTRIBUTION STATEMENT A.
APPROVED FOR PUBLIC RELEASE; DISTRIBUTION UNLIMITED.

13. SUPPLEMENTARY NOTES

This work is declared a work of the U.S. Government and is not subject to copyright protection in the United States.

14. ABSTRACT

Electromagnetic materials characterization is important in the design of systems that interact with electromagnetic waves. Determining the constitutive parameters of a material is a vast area of research and practice. For this paper, discussion will focus on a destructive method using waveguides in the frequency range of 6-18 GHz. Traditional methods to perform similar measurements include using coaxial cable, stripline, focus beam and rectangular waveguides. This work will use Double Ridged Waveguide (DRWG) to compare to these other methods and will discuss the attributes and drawbacks of this new approach. The most similar method utilizes rectangular waveguide, so the primary focus will be on comparisons this method with DRWG. The significant advantage to using DRWG is the increase in available measurement bandwidth. The challenges include sample fabrication and increased mathematical difficulty in finding the cutoff frequency for DRWG. These challenges are addressed and measurement results are examined.

15. SUBJECT TERMS

material characterization, double ridged waveguide, constitutive parameters, electromagnetics

16. SECURITY CLASSIFICATION OF:			17. LIMITATION OF ABSTRACT	18. NUMBER OF PAGES	19a. NAME OF RESPONSIBLE PERSON
a. REPORT	b. ABSTRACT	c. THIS PAGE			Dr. Michael J. Havrilla (ENG)
U	U	U	UU	83	19b. TELEPHONE NUMBER *(include area code)* (937) 255-3636 x4582 michael.havrilla@afit.edu

Standard Form 298 (Rev. 8–98)
Prescribed by ANSI Std. Z39.18